國立臺灣大學理學院物理學系研究所

碩士論文

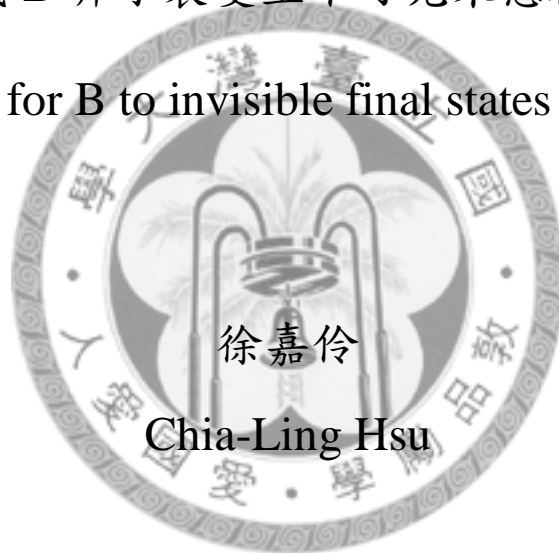Graduate Institute of Physics

College of Science

National Taiwan University

Master Thesis

尋找 B 介子衰變至不可見末態粒子

Search for B to invisible final states at Belle
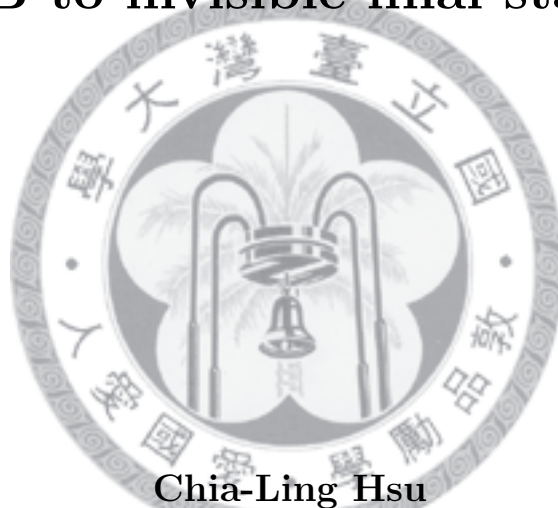
徐嘉伶

Chia-Ling Hsu

指導教授：張寶棣 王名儒 教授

Advisor: Prof. Paoti Chang, Min-Zu Wang

中華民國一百年六月

June, 2011

Department of Physics

College of Science

National Taiwan University

Master Thesis

Search for B to invisible final states at Belle

Chia-Ling Hsu

Department of Physics, National Taiwan University,
Taipei, Taiwan, R.O.C.

Advisor
Prof. Paoti Chang
Prof. Min-Zu Wang
Department of Physics, National Taiwan University,
Taipei, Taiwan, R.O.C.

June 2011

Abstract

We report a new search for B decays into invisible final states using a data sample of 657 million $B\overline{B}$ pairs collected at $\Upsilon(4S)$ resonance with the Belle detector at the KEKB $e^+ - e^-$ collider. The $\nu\bar{\nu}$ signals are identified by fully reconstructing the accompanying B mesons and requiring no other charged particles and no extra energy deposited in the calorimeter. By performing maximum likelihood fits to the reconstructed candidates, no significant signal is observed and we set the upper limit on the branching fraction $\mathcal{BF}(B \to invisible) < 1.3 \times 10^{-4}$ at the 90% confidence level.

Acknowledgement

Contents

List of Figures

List of Tables

Chapter 1

Introduction

1.1 Particle Physics

People have quested for "What's the universe made of?" due to the curiosity of human beings. At the fifth century BC, the Greek philosopher Leucippus and his student Democritus proposed that the world was made of atoms, which means uncuttable.

In the early 19th century, John Dalton presented Atomic Theory, in which he claimed that all matter is composed of atoms with definite weights. Although at that time, the atoms could not be observed directly since the limitation of technology, Atomic Theory predicted some concrete characteristics based on experiments. After few decades, Mendelevee presented a periodic table of elements on which the elements were arranged according to their chemical properties. The regularity in the periodic table indicates that the elements might be made of smaller particles.

Till the discovery of electron in 1897 by J.J. Thomson, atoms were regarding as the fundamental particles. In few decades, the discoveries of proton and neutron by Ernest Rutherford and Sir James Chadwick. The three types of particles construct an atom, it seems the question of foundation of matter was done.

Yet, a question exists in the nucleus: What kind of force is holding protons and neutrons in a nucleus? Hideki Yukawa proposed the theory of mesons and predicted the existence of mesons in 1935. In the theory of mesons, mesons are interchanged by nucleons to provide the needed force. The pion meson (π) was discovered about 10 years later. The prediction and existence of a subatomic particle led to a rapid development of particle physics, and more and more kinds of particle had been found in the following decades.

In the past, particle physicists only could do experiments via the high energy cosmic rays, which are uncontrollable and low-rated. The energetic cosmic rays might scatter particles in the atmosphere, and such interaction could produce some subatomic particles. To provide a controllable interaction source, scientist started building particle accelerators to propel charged particle(electrons, positrons or protons) to high energy, then collide with a target or another energetic particle beam.

1.2   The Standard Model

The Standard Model (SM) of particle physics is the theory concerning the characteristics and interactions of fundamental particles. It's one of most successful theories which has passed numerous experimental tests. In the Standard Model, the elemental particles are classified in three classes: 6 kinds of quarks, 6 kinds of leptons and 4 kinds of force carriers. Based on the Standard Model, all matter consists of quarks and leptons. The quarks carry fractional unit charges - $+2/3$ or $-1/3$, and leptons carry integral charge. Both of them are spin-1/2 particles (fermions), and can be classified as three generations. The properties of fermions are shown in Table 1.1. The force carriers are exchanged between particles, causing the interactions: photons for the electromagnetic force, $W^{\pm}$ and Z bosons for the weak interaction, three colors of gluon for the strong interaction. Still, the Standard Model is not a complete theory of fundamental interaction because it does not incorporate the physics of general relativity, such as gravitation and dark energy.

Table 1.1: Organization of Leptons and Quarks.[1]

		Name	Symbol	Charge(e)	Mass(MeV/c^2)
First generation	Quark	Up	u	$+\frac{2}{3}$	$1.5 - 3.3$
		Down	d	$-\frac{1}{3}$	$3.5 - 6.0$
	Lepton	Electron	e	-1	0.511
		Electron neutrino	ν_e	0	< 0.0000022
Second generation	Quark	Charm	c	$+\frac{2}{3}$	$1160 - 1340$
		Strange	s	$-\frac{1}{3}$	$70 - 130$
	Lepton	Muon	μ	-1	105.7
		Muon neutrino	ν_μ	0	< 0.17
Third generation	Quark	Top	t	$+\frac{2}{3}$	$169100 - 173300$
		Bottom	b	$-\frac{1}{3}$	$4130 - 4370$
	Lepton	Tau	τ	-1	1777
		Tau neutrino	ν_τ	0	< 15.5

Table 1.2: Properties of Mediators. [1]

Mediator	Charge(e)	Mass(GeV/c^2)	Interaction
Gluon(g)	0	0	strong
Photon(γ)	0	0	electromagnetic
$W^\pm$	± 1	80.4	(charged) weak
Z^0	0	91.2	(neutral) weak

1.2.1 CP Violation

The origin of the universe is generally believed to start from the Big Bang. According to Einstein's mass-energy equivalence formula: $E = mc^2$, the matter and anti-matter should be equally produced from energy. In the other words, there should be equal amount of matter and anti-matter in the world, contrary to reality, the universe is chiefly made of matter rather than consist of equal parts of matter and anti-matter.

In 1967, Andrei Sakharov proposed three necessary conditions for producing matter and anti-matte at different rate[2]. The three necessary Sakharov condition are:

- Baryon number violation.

- CP-symmetry violation.

- Interaction out of thermal equilibrium.

The C stands for the charge conjugate operator, which transforms a particle into anti-particle, and the P stands for the parity operator, which creates the mirror image of a physical system. Until 1956, parity conservation was believed to be one of the fundamental conservation law. T.-D. Lee and C.-N. Yang revealed that while parity conservation had been proved in the decay via the strong or electromagnetic interactions, it was unverified in the weak interaction [3]. Soon, the parity violation was discovered in the β decay of Co-60 nuclei experiment conducted by C.-S. Wu in 1957 [4]. The CP symmetry was also believed to be a conserved quantity until the violation of CP symmetry was first observed in the decays of neutral kaon system by Cronin and Fitch in 1964 [5]. However the violation of CP symmetry is small in the kaon system, the order of 10^{-3} only, it's insufficient to explain the asymmetry of matter and anti-matter in the universe.

The violation of CP symmetry is incorporated in the Standard Model by including

the complex phase in the CKM matrix to describe quark mixing.

1.2.2 CKM Matrix

The quark can change its flavor to another generation in the weak interaction, its mass eigenstate is different from the weak interaction state. N. Cabibbo introduced a angle θ_c, which is called the Cabibbo angle, to transform the mass eigenstates to the weak interaction eigenstates [6]. In order to explain the CP violation in the weak interaction, M. Kobayashi and T. Maskawa generalized the Cabibbo matrix into the Cabibbo-Kobayashi-Maskawa (CKM) matrix by introducing a complex term into the mixing matrix which also predicts the existence of third generation of quarks [7]. The CKM matrix is unitary, and can be represented as

$$\begin{pmatrix} d' \\ s' \\ b' \end{pmatrix} = \mathbf{V_{CKM}} \begin{pmatrix} d \\ s \\ b \end{pmatrix} = \begin{pmatrix} V_{ud} & V_{us} & V_{ub} \\ V_{cd} & V_{cs} & V_{cb} \\ V_{td} & V_{ts} & V_{tb} \end{pmatrix} \begin{pmatrix} d \\ s \\ b \end{pmatrix}, \tag{1.1}$$

where the elements are the coupling strength between quarks and W-boson. The values of elements are determined by weak decays of the relevant quarks.

1.3 $\Upsilon(4S)$ and B meson

In the year of 1977, a new resonance named Υ, which turns out to be a flavorless meson formed by a third generation quark and it's anti-quark, was discovered by E288 at Fermilab [8]. The first third generation, and fifth quark discovered, was named bottom. In the following years, three more resonances, $\Upsilon(2S)$, $\Upsilon(3S)$, and $\Upsilon(4S)$, were found [9] [10]. In these resonances, $\Upsilon(4S)$ should be mentioned for its mass above the threshold of $B\overline{B}$ pair, which means abundant B meson can be obtained via the $\Upsilon(4S)$ decay. The branching fraction of $\Upsilon(4S) \to B^+B^-$ is the same as $\Upsilon(4S) \to B^0\overline{B^0}$.

In the Standard Model, B mesons are the bound states of a $\overline{b}$ quark and either an

Table 1.3: Properties of B mesons.

Type	Constituents	Mass(MeV/c^2)	Lifetime(ps)
B^+	$u\bar{b}$	5279.1 ± 0.4	1.643 ± 0.010
B^0	$d\bar{b}$	5279.3 ± 0.7	1.527 ± 0.008
B_s^0	$s\bar{b}$	5369.6 ± 2.4	1.454 ± 0.040
B_c^+	$c\bar{b}$	6286.0 ± 5.0	0.469 ± 0.065

u (B^+), d (B^0), s (B_s^0) and c quark (B_c^+). The properties of B meson are shown in Table 1.3. B mesons mainly decay via $b \to c$ transition. The decay modes of B mesons which do not occur through $b \to c$ transition are called rare B decays. The rare decays are suppressed by the element V_{ub} in CKM matrix and are good probes for CP asymmetry and new physics. However, the branching fractions are very small in rare B decays, and the efficiency from the final state back to B mesons are also relatively low. To measure the CP violations in B mesons, KEK(Tsukuba, Japan) and SLAC(California, USA) built energy-asymmetry e^+e^- colliders, which have been designed to produce a large number of B mesons.

1.4 Motivation

The products of invisible B^0 decays are particles neither charged nor detected by an electromagnetic calorimeter. Therefore the products can be neutrinos or some hypothetical particles(such as neutralino, $\widetilde{\chi}_1^0$) [11] [12] [13].

According to the Standard Model, the $B^0 \to \nu\bar{\nu}$, which would give such an invisible experimental signature, is strongly helicity-suppressed by a factor of order $(m_\nu/m_{B^0})^2$[14].

The branching fraction for $B^0 \to \nu\bar{\nu}$ is given by Buchalla and Buras(1993)

$$\mathcal{B}(B^0 \to \nu\bar{\nu}) = \tau_{B^0} \frac{G_F^2}{\pi} \left(\frac{\alpha}{4\pi \sin^2 \Theta_W} \right)^2 F_{B^0}^2 m_\nu^2 m_{B^0}$$
$$\times \sqrt{1 - 4m_\nu^2/m_{B^0}^2} |V_{tb}^* V_{td}|^2 Y^2(x_t), \tag{1.2}$$

where G_F is the Fermi coupling constant and τ_B is the life time of B^0. The Feynman diagrams for the $B^0 \to \nu\bar{\nu}$ decay in the Standard Model are shown in Fig. 1.1.

However, some new physics models can enhance the branching fraction for this type of decay models by orders of magnitude. A phenomenological model relates to R-parity violation allows for an invisible B^0 decay to a $\bar{\nu}\tilde{\chi}_1^0$ with a branching fraction in the order of 10^{-6} to 10^{-7}, the process for the $B^0 \to \bar{\nu}\tilde{\chi}_1^0$ are shown in Fig. 1.2[15].

The current upper limit of branching fraction set by the Babar Collaboration is 22×10^{-5} in 2004 [16] [17].
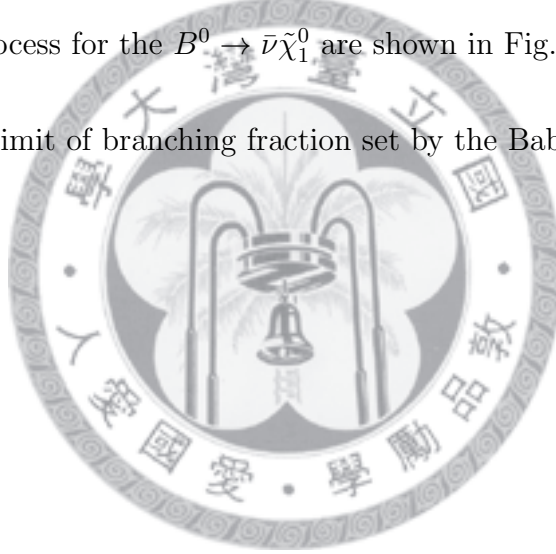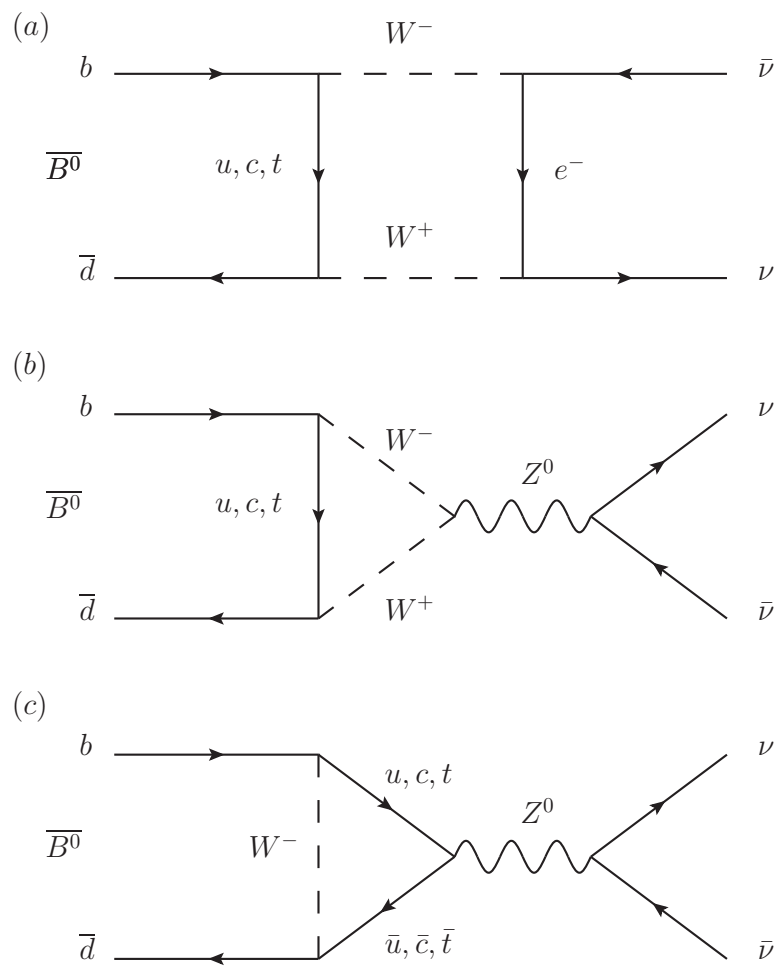
Figure 1.1: Feynman diagrams for $B^0 \to \nu\bar{\nu}$ decay in the Standard Model.
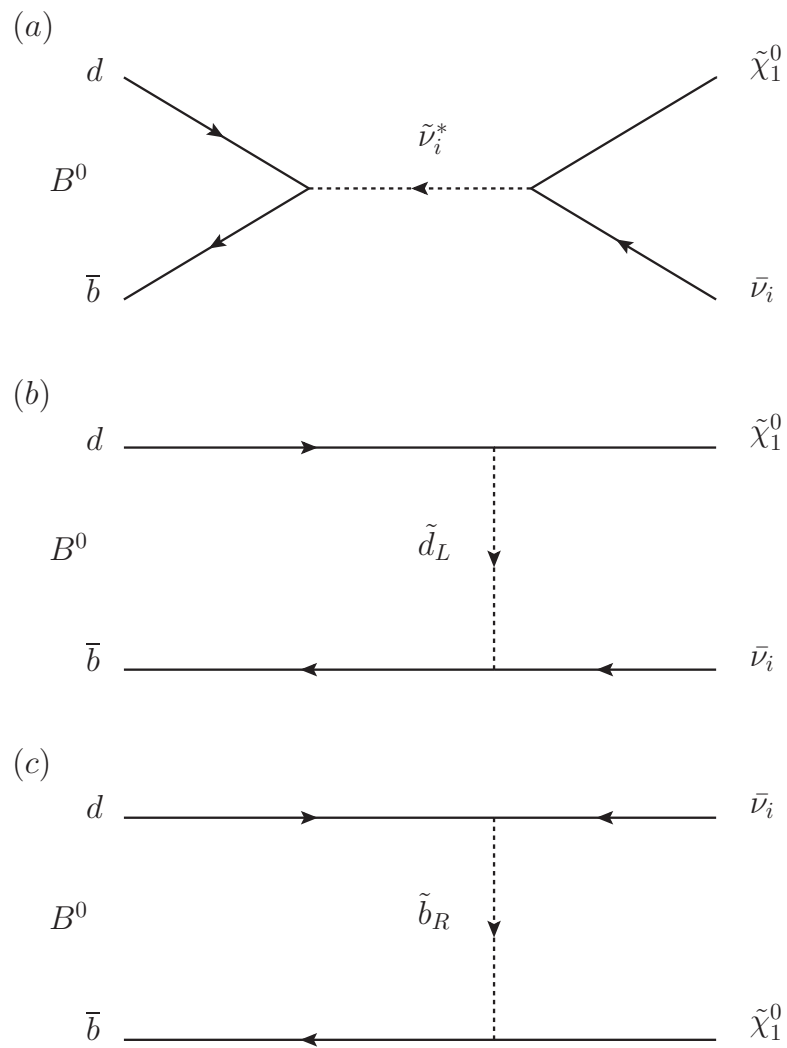
Figure 1.2: Feynman diagrams for $B^0 \to \bar{\nu}\tilde{\chi}_1^0$ decay in the R-parity violation model.

Chapter 2

B Factary at KEK

2.1   Introduction

KEK is the research organization for high-energy physics in Tsukuba, Japan. The Belle experiment is one of projects in KEK, the main goal is to study the CP violation. There are two major facilities in the Belle experiment, the KEKB accelerator (Fig. 2.1) and the Belle detector (Fig. 2.2).

The KEKB accelerator is designed to produce B meson pairs efficiently. Hence the Belle experiment is known as a B-factary.

2.2   KEKB accelerator

The KEKB accelerator is operating with two storage rings: a low-energy ring (LER) for positrons with 3.5 GeV and a high-energy ring (HER) for electrons with 8.0 GeV. The two energy-asymmetry beams collide at the interaction point (IP) with a crossing angle of ± 11 mrad. The finite crossing angle is designed to reduce parasitic collisions near the interaction point, it's also to eliminate the beam separation-bend procedure and provide higher luminosity. The center-of mass(CM) energy is 10.58 GeV at the $\Upsilon(4S)$ resonance, which is just above the production threshold to $B\overline{B}$. At this energy, the cross section
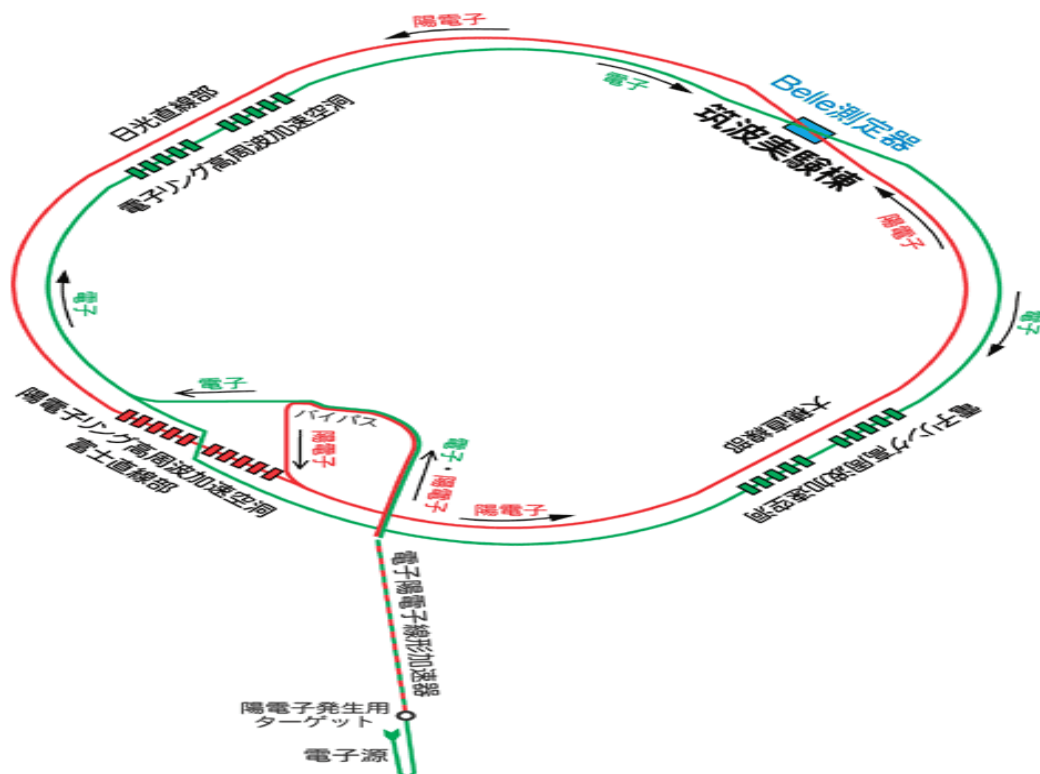
Figure 2.1: The configuration of the KEKB accelerator.
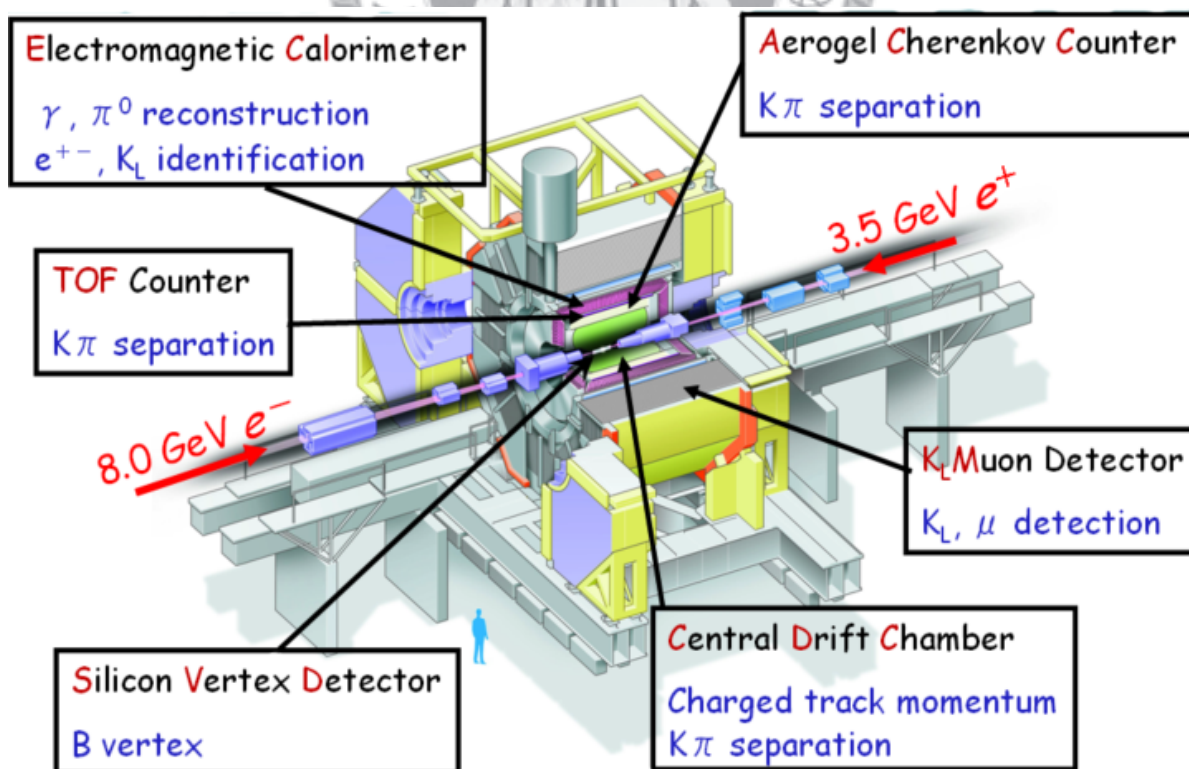
Figure 2.2: Overall view of Belle detector.

$\Upsilon(4S) \to B\overline{B}$ is 1.05 nb, and the continuum process $e^+e^- \to q\overline{q}$ (q=u,d,s, and c) has a cross section of 3.7 nb.

The flight length of a B meson in the CM frame of $\Upsilon(4S)$ is 2 μm, this distance is not enough for a time-dependent CP analysis. Therefore, the asymmetric beam energy provide a Lorentz boost with a factor $\beta\gamma \sim 0.425$ for B mesons. The average distance between decay vertex of the two B mesons in the beam direction(the z axis) is about 200 μm. The resolution of the silicon vertex detector is suffciently good to measure the separation. The KEKB is designed to operate with a peak luminosity of 10^{34}cm^{-2}s, corresponding $\sim 10^8$ $B\overline{B}$ pairs per year. The parameters for the KEKB accelerator and Belle detector are shown in Table 2.1 and Table 2.2. More details of the Belle detector can be found from the reference [18].

2.3 The Beam Pipe

A main requirement of the Belle detector is precise measurement of B meson decays. In order to achieve this goal, the silicon vertex detectors (SVD) should be close to the interaction point (IP). Therefore, a thin beam pipe with a small vertex detector is preferred. The designed beam pipe has an inner radius of 2.0 cm, and an outer wall 2.3 cm in radius. The central part (-4.6 cm $\leq z \leq 10.1$ cm) of the beam pipe consists of double beryllium cylinders of 0.5 mm thickness. The gap between these two beryllium walls provides a channel for helium gas, which is used to be cooling. Figure 2.3 shows the cross-section of the beryllium beam pipe. The maximum temperature increase for the inner beryllium is estimated to be 25 degrees assuming a uniformly distributed 100W heat load on the inner wall and a 2 g/s He flow. The beryllium central section is brazed to aluminum pipes which allows the synchrotron x-rays generated in the QCS and QC1 magnets to pass through without hitting the inner beryllium wall. A mask of gold is used to absorbed the back-scattered photons which have a critical energy less than 2 KeV.

Table 2.1: Design parameters of the KEKB accelerator.

Ring		LER	HER	Unit
Energy	E	3.5	8.0	GeV
Circumference	C	3016.26		m
Luminosity	L	1×10^{34}		$cm^{-2}s^{-1}$
Crossing angle	θ_x	± 11		mrad
Tune shifts	ξ_x/ξ_y	0.039/0.052		
Beta function at IP	β_x^*/β_y^*	0.33/0.01		m
Beam current	I	2.6	1.1	A
Natural bunch length	σ_z	0.4		cm
Energy spread	σ_ε	7.1×10^{-4}	6.7×10^{-4}	
Bunch spacing	s_b	0.59		m
Particles/bunch	N	3.3×10^{10}	1.4×10^{10}	
Emittance	$\varepsilon_x/\varepsilon_y$	$1.8 \times 10^{-8}/3.6 \times 10^{-10}$		
Synchrotron	ν_s	$0.01 \sim 0.02$		
Betatron tune	ν_x/ν_y	45.52/45.08	47.52/43.08	
Momentum compaction factor	α_p	$1 \times 10^{-4} \sim 2 \times 10^{-4}$		
Energy loss/turn	U_0	$0.81^\dagger/1.5^{\dagger\dagger}$	3.5	MeV
RF voltage	V_c	$5 \sim 10$	$10 \sim 20$	MV
RF frequency	f_{RF}	508.887		MHz
Harmonic number	h	5120		
Longitudinal damping time	τ_ε	$43^\dagger/23^{\dagger\dagger}$	23	ms
Total beam power	P_b	$2.7^\dagger/4.5^{\dagger\dagger}$	4.0	MW
Radiation power	P_{SR}	$2.1^\dagger/4.0^{\dagger\dagger}$	3.8	MW
HOM power	P_{HOM}	0.57	0.15	MW
Bending radius	ρ	16.3	104.5	m
Length of bending magnet	l_B	0.915	5.86	m

†: without wigglers, ††: with wigglers

Table 2.2: Performance parameters for the Belle detector. There were two configurations of inner detectors used to collect two data sets, DS-I and DS-II, corresponding to a 3-layer SVD1 and a 4-layer SVD2 with a smaller beam pipe, respectively.

Detector	Type	Configuration	Readout	Performance
Beam pipe DS-I	Beryllium double wall	Cylindrical, r = 20mm, 0.5/2.5/0.5(mm) = Be/He/Be w/ He gas cooled		
Beam pipe DS-II	Beryllium double wall	Cylindrical, r = 15mm, 0.5/2.5/0.5(mm) = Be/PF200/Be		
EFC	BGO	Photodiode readout Segmentation : 32 in ϕ; 5 in θ	160×2	Rms energy resolution: 7.3% at 8 GeV 5.8% at 2.5 GeV
SVD1	Double-sided Si strip	3-layers: 8/10/14 ladders Strip pitch: 25(p)/50(n)μm	ϕ: 40.96k z: 40.96k	$\sigma(z_{CP}) \sim 78.0\mu m$ for $B \to \phi K_s^0$
SVD2	Double-sided Si strip	4-layers: 6/12/18/18 ladders Strip pitch: 75(p)/50(n)μm (layer1-3) 73(p)/65(n)μm (layer4)	ϕ: 55.29k z: 55.296k	$\sigma(z_{CP}) \sim 78.9\mu m$ for $B \to \phi K_s^0$
CDC	Small cell drift chamber	Anode: 50 layers Cathode: 3 layers r = 8.3 - 86.3 cm $-77 \leq z \leq 160$ cm	Anode: 8.4k Cathod: 1.8k	$\sigma_{r\phi} = 130\mu m$ $\sigma_z = 200 \sim 1400\mu m$ $\sigma_{Pt}/Pt = 0.3\%\sqrt{p_t^2+1}$ $\sigma_{dE/dx} = 0.6\%$
ACC	Silica aerogel	960 barrel/228 end-cap FM-PMT readout		$N_{p.e.} \geq 6$ K/π seperation: $1.2 < p < 3.5$GeV/c
TOF TSC	Scintillator	128 ϕ segmentation r = 120 cm, 3-cm long 64 ϕ segmentation	128×2 64	$\sigma_t = 100$ ps K/π seperation: up to 1.2 GeV/c
ECL	CsI (Towered-structure)	Barrel: r = 125 - 162 cm End-cap: z = -102 cm and +196cm	6624 1152(F) 960(B)	$\sigma_E/E = 1.3\%/\sqrt{E}$ $\sigma_{pos} = 0.5$ cm$/\sqrt{E}$ (E in GeV)
KLM	Resistive plate counters	14 layers (5 cm Fe + 4cm gap) 2 RPCs in each gap	θ: 16k ϕ: 16k	$\Delta\phi = \Delta\theta = 30$mr for K_L $\sim 1\%$ hadron fake
Magnet	Supercon.	Inner radius = 170 cm		B=1.5T

Particle backgrounds are critical at KEKB. The rate of particles from both beams hitting the beam pipe is calculated to be around 130 kHz in a 10^{-9} Torr vacuum. Movable masks are installed to reduce the radiation levels at injection.
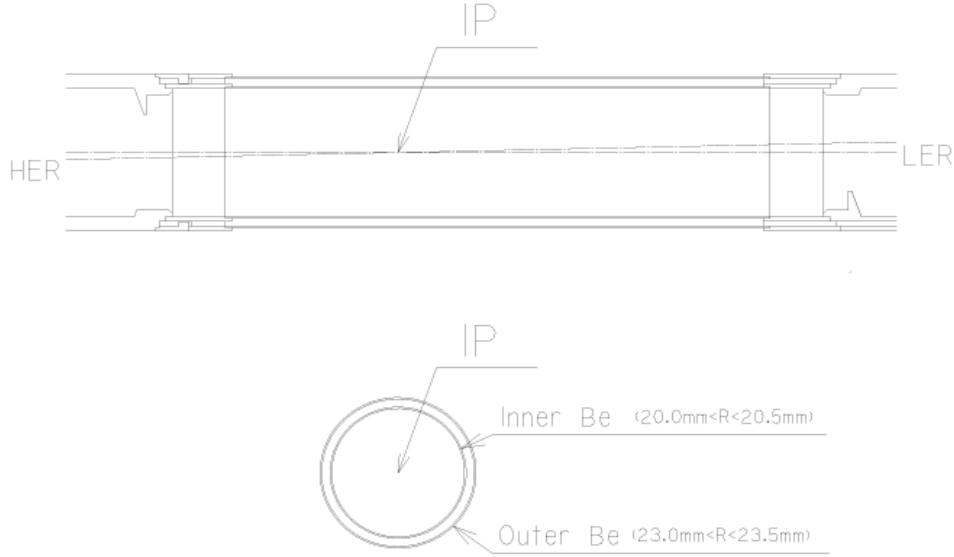
Figure 2.3: The graphical illustration of the beam pipe.

2.4   Silicon Vertex Detector (SVD)

The Silicon Vertex Detector (SVD) is primarily for the measurement of the decay vertices of B mesons and contributing to the tracking [19]. The information of the decay vertices is very important for observation of time-dependent CP asymmetries in B meson decays. The first version of SVD (SVD1) consists of three layers of double-sided silicon strip detector (DSSD), comprising 8, 10, 14 ladders in the inner, middle and outer layers. The radii of these layers are 30 mm, 45.5 mm and 60.5 mm. It covers $23° < \theta < 139°$, corresponding to 86% coverage of solid angle. The radii of these layers are 30 mm, 45.5 mm, and 60.5 mm. The DSSDs were developed for the DELPHI micro-vertex detector In each DSSD, there are 1280 striped sensors and 640 readout pads on both opposite sides. The z-strip (ϕ-strip) pitch is 42 (25) μm, and readout z-strip (ϕ-strip) pitch is 84 (50) μm, respectively. The size of the active region in DSSD is 53.5×32.0 mm^2 on the z-side

and 54.5×32.0 mm^2 on the ϕ-side.

In summer 2003, a new vertex detector replaced SVD1 successfully, called SVD2. The SVD2 consists of four detector layers, comprising 6, 12, 18 and 18 ladders in the first, second, third and forth layer, respectively. The SVD2 also have larger coverage than SVD1, $17° < \theta < 150°$, which is the same as CDC. The beam pipe is replaced by a smaller(1.5 cm in radius) one. The radii of the four layers are 20, 43.5, 70 and 80 mm, respectively. This design improves the vertex resolution. The side-view of SVD1 and SVD2 are shown in Fig 2.4.

2.5   Extreme Forward Calorimeter (EFC)

The extreme forward calorimeter (EFC) is designed to improve on luminosity monitoring and further extend the polar angle covers by ECL ($17° < \theta < 150°$). Photons and electrons are detected by the EFC at the extreme forward and backward area which ECL do not cover. The EFC covers the range of polar angle $6.4° < \theta < 11.5°$ in the forward direction and $163.3° < \theta < 171.2°$ in the backward direction. The extended coverage can improve the sensitivity to two-photon physics and $B \to \tau\nu$ decay. Due to the highly exposure of radiation, the material of EFC is radiation-hard BGO (Bismuth Germanate, $Bi_4Ge_3O_{12}$). The BGO crystals are considered to be stable in highly radiation condition. Figure 2.5 illustrates the isometric view of the BGO crystal.

2.6   Central Drift Chamber (CDC)

The Central Drift Chamber (CDC) is used to reconstruct charged tracks passing through the region of its coverage, $17° < \theta < 150°$, and provide information of the momentum and energy deposition(dE/dx) of charged tracks. The curvatures of transverse plane can be used to determined the transverse momentum (p_T) from a charged particle,
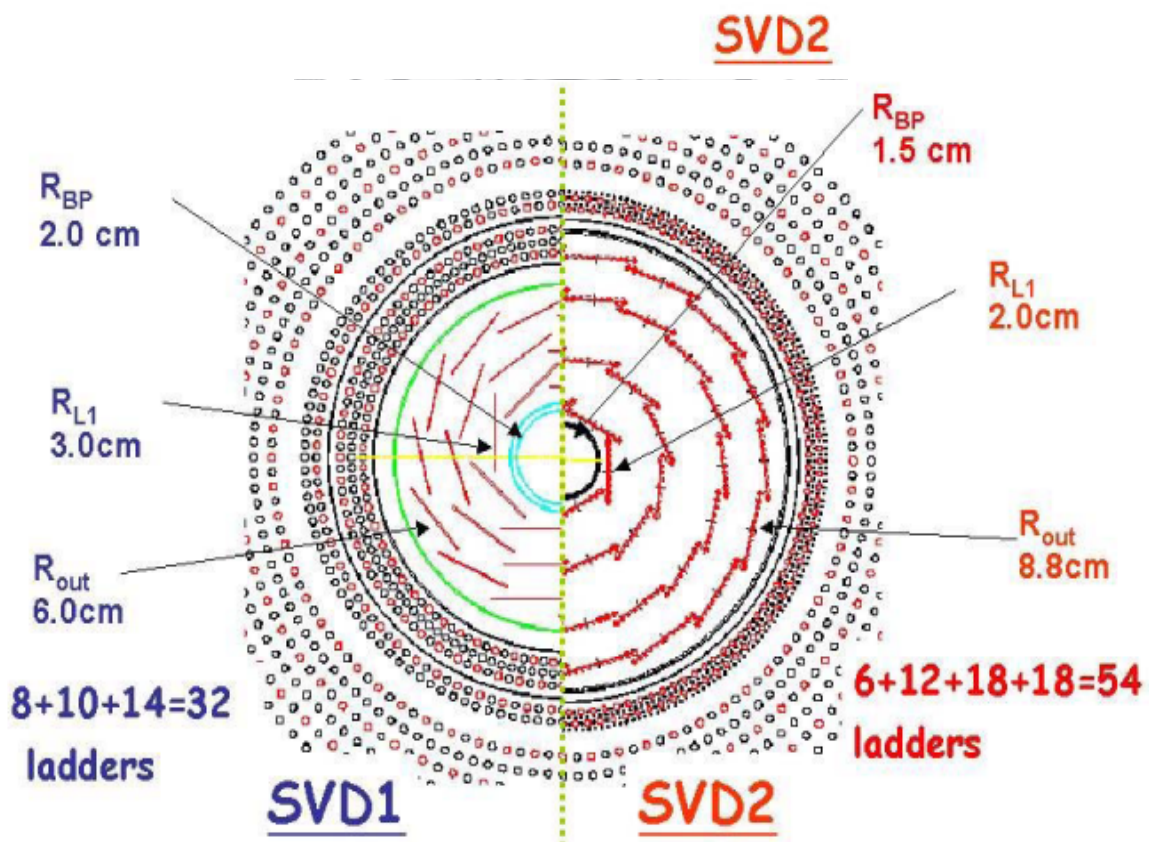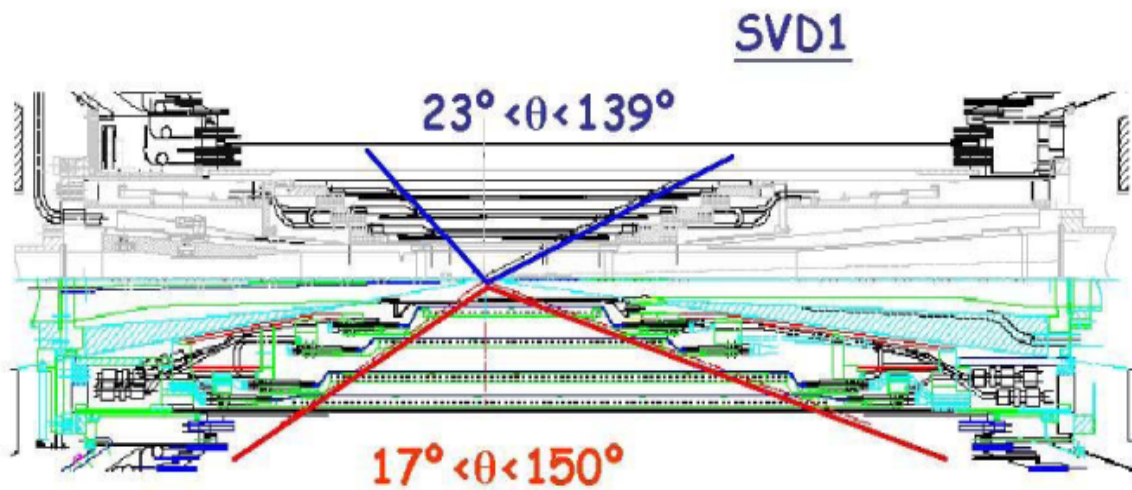
Figure 2.4: The graphical illustration of sub-detector SVD1 and SVD2.
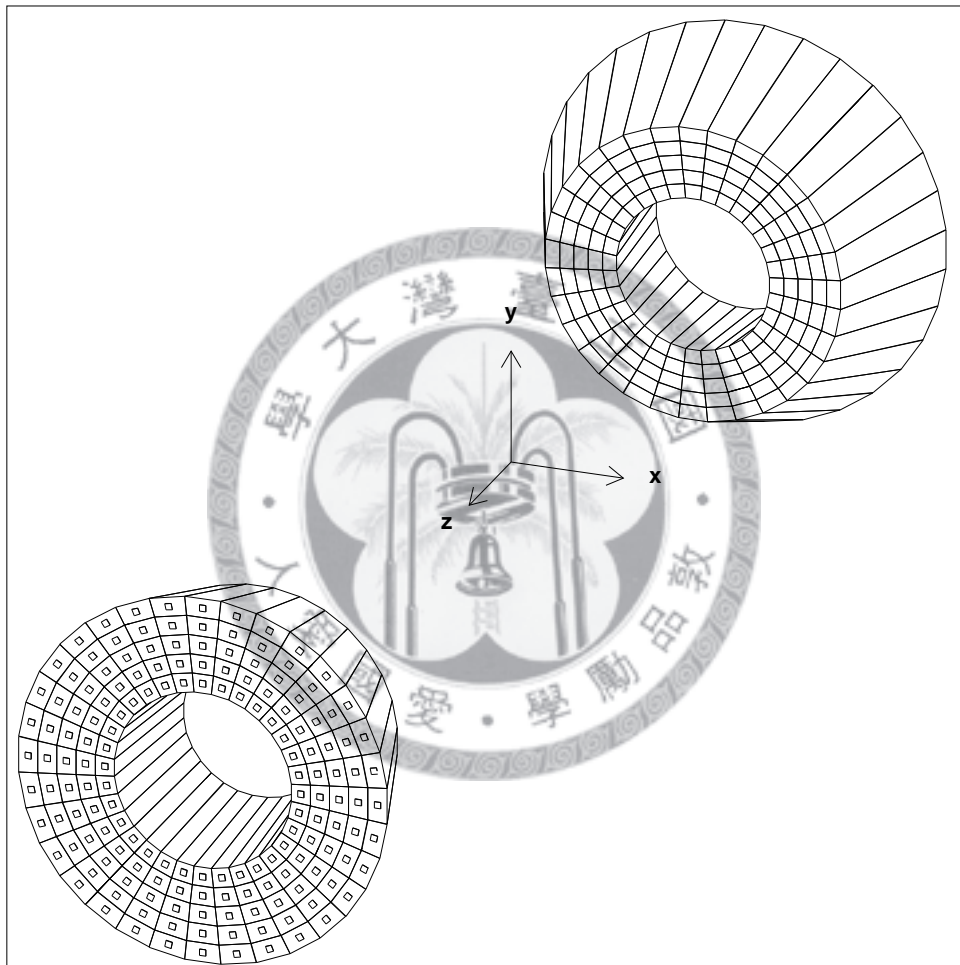
Figure 2.5: The isometric view of the forward and backward EFC detectors, the BGO crystals and the location of photodiodes are illustrated.

combined with the helical track information, the momentum of z direction could also be obtained. This sub-detector is designed to fulfill the requirement of momentum resolution of $\sigma_{p_T}/p_T \sim 0.005\sqrt{1 + p_T^2}$ (p_T in GeV/c) for all charged particles with $p_T < 100$ MeV/c.

The CDC consists of 50 cylindrical layers and 3 cathode strip layers, and has 8400 drift cells. The structure of CDC and cell are shown in Fig. 2.6 and Fig. 2.7.

Since the majority of the B decay daughters have a momenta lower than 1 GeV/c, the minimization of multiple Column scattering is important for improving the momentum resolution. We choose a low-Z gas, such as 50% helium and 50% ethane mixture, to reduce multiple scattering and background from synchrotron radiation. Moreover, the large portion of ethane provides a good dE/dx resolution, which is useful in the particle identification especially for the separation of kaons (K) and pions (π) in the momentum region below 0.5 GeV/c. Figure 2.8 shows a plot of dE/dx and particle momentum, together with the expected truncated mean.

Figure 2.6: Overview of the CDC structure. The unit in the figure is mm.

Figure 2.7: CDC cell structure.
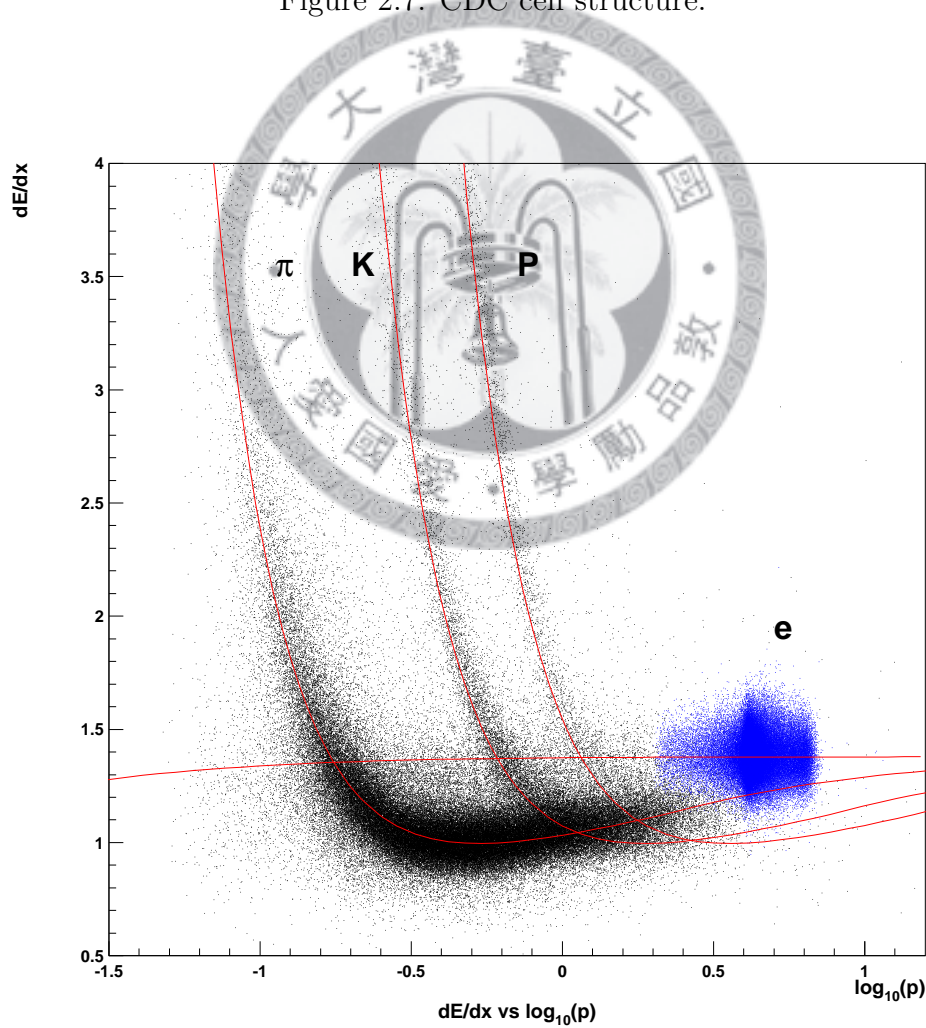
Figure 2.8: The plot of dE/dx and particle momentum, together with the expected truncated mean.

2.7 Aerogel Čerenkov Counter (ACC)

The Aerogel Čerenkov Counter (ACC) is used to distinguish $\pi^{\pm}$ and $K^{\pm}$ in the further extensive momentum region (1.2 GeV/c $\sim$ 4.0 GeV/c) by the Čerenkov light. The Čerenkov light is the photons which is emitted by the charged particles exceeds the speed of light in a medium. The phenomenon will take place if the velocity of particle, β, satisfies

$$n > 1/\beta = \sqrt{1 + (m/p)^2} \tag{2.1}$$

where n is the refractive index of the medium, m is the mass of the particle and p is the momentum of the particle.

The ACC is divided into two parts, barrel and end-cap. The barrel part consists of 960 aerogel counter module segmented into 60 cells in ϕ direction, covering the polar angle of 33.3° to 127.9°, and the end-cap part comprises 288 modules arranged in 5 concentric layers, covering the polar angle of 13.6° to 33.4°. The side-view of the full ACC system is shown in Fig. 2.9. All aerogel counters are arranged in a semi-tower geometry, pointing to the IP. The finemesh photomultiplier tubes (FM-PMTs) are used to detector Čerenkov light since it can operate in strong magnetic field. The refractive indices are chosen to be between 1.01 to 1.03 depending on their polar angle region. Figure 2.10 shows two types of unit module.

2.8 Time of Flight (TOF)

The time-of-flight (TOF) detector system shown in Fig. 2.11 provides an powerful identification method for particle with small momentum. For a 1.2 m flight path, a system of counters with 100 ps time resolution is effective for particle momenta below about 1.2 GeV/c, which encompasses 90% of the particles produced in $B\overline{B}$ decays. The
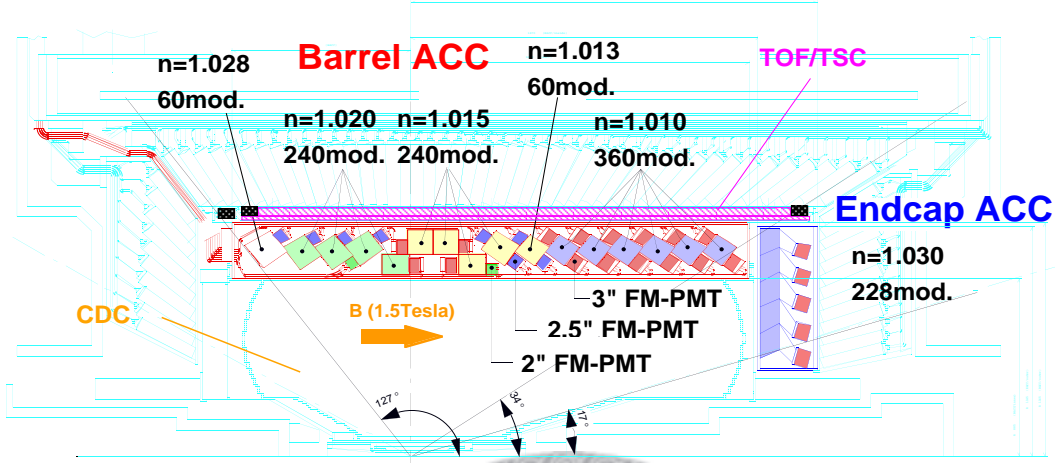
Figure 2.9: Sideview of ACC system, together with other nearby detectors, the index of refraction (n) is also given for each ACC module.

system functions with the concept of TOF that if the time T, the flying path L and the momentum p are measured, the mass m of a particle can be obtained from the following equation:

$$T = \frac{L}{c}\sqrt{1 + \frac{m}{p}c^2}. \tag{2.2}$$

When $E >> mc^2$, the relation of time difference for two particles of different masses is:

$$\Delta T = T_1 - T_2 \approx \frac{Lc}{2p^2}(M_1^2 - M_2^2). \tag{2.3}$$

where $M_{1(2)}$ is the mass of the first (second) particle. The measurement of ΔT can provide good K/π separation for the low momentum particles.

a) Barrel ACC Module
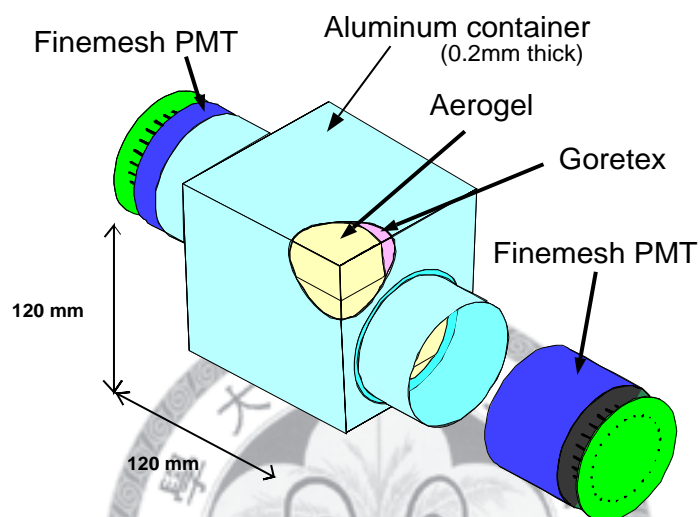
b) Endcap ACC Module
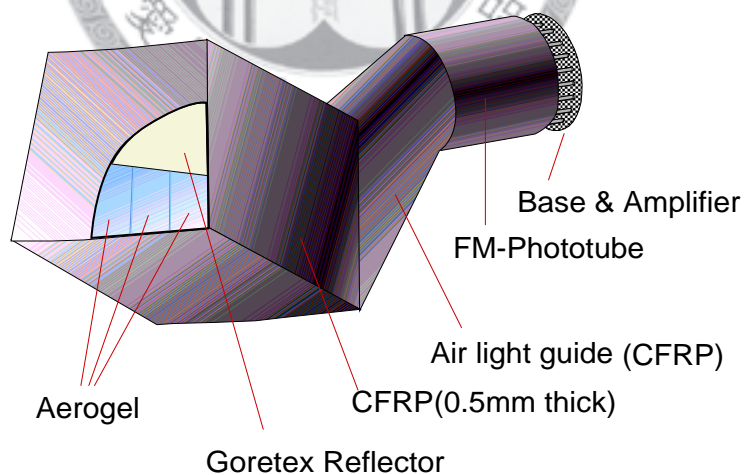
Figure 2.10: Schematic drawing of a typical ACC counter module: (a) barrel and (b) end-cap ACC.
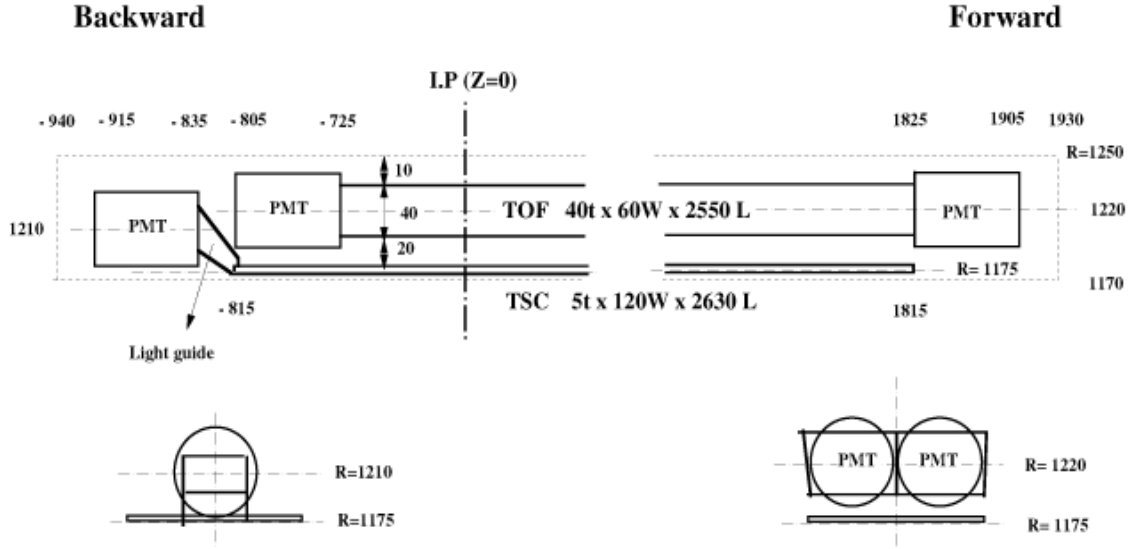
Figure 2.11: An illustration of a TOF/TSC module. The unit of the figure is in mm.

2.9 Electromagnetic Calorimeter (ECL)

The purpose of the Electromagnetic Calorimeter (ECL) is to detect the photons from B meson decays with high efficiency and good energy resolution. Most of the photons are end-products of decay cascades and have relatively low energy, thus, good performance with photons below 500 MeV is necessary. Besides these cascade photons, important two-body decay modes such as $B \to K^* \gamma$ and $B^0 \to \pi^0 \pi^0$ require a good energy resolution up to 4 GeV, which are also needed to reduce backgrounds for these modes. Electron identification in Belle depends primarily on a comparison of the momentum of charged tracks and the energy deposits in the ECL crystals. Good electromagnetic energy resolution results in better hadron rejection. High momentum π^0 detection requires good resolution of positions for two nearby photons and a precise determination of their opening angle. All of these require a fine-grained segmentation in the calorimeter.

In order to satisfy above requirements, ECL consists of a high segmented array of CsI(Tl) crystals with silicon photodiode readout installed inside the coil of solenoid magnet. Figure 2.12 shows the configuration of the ECL.

BELLE CsI ELECTROMAGNETIC CALORIMETER
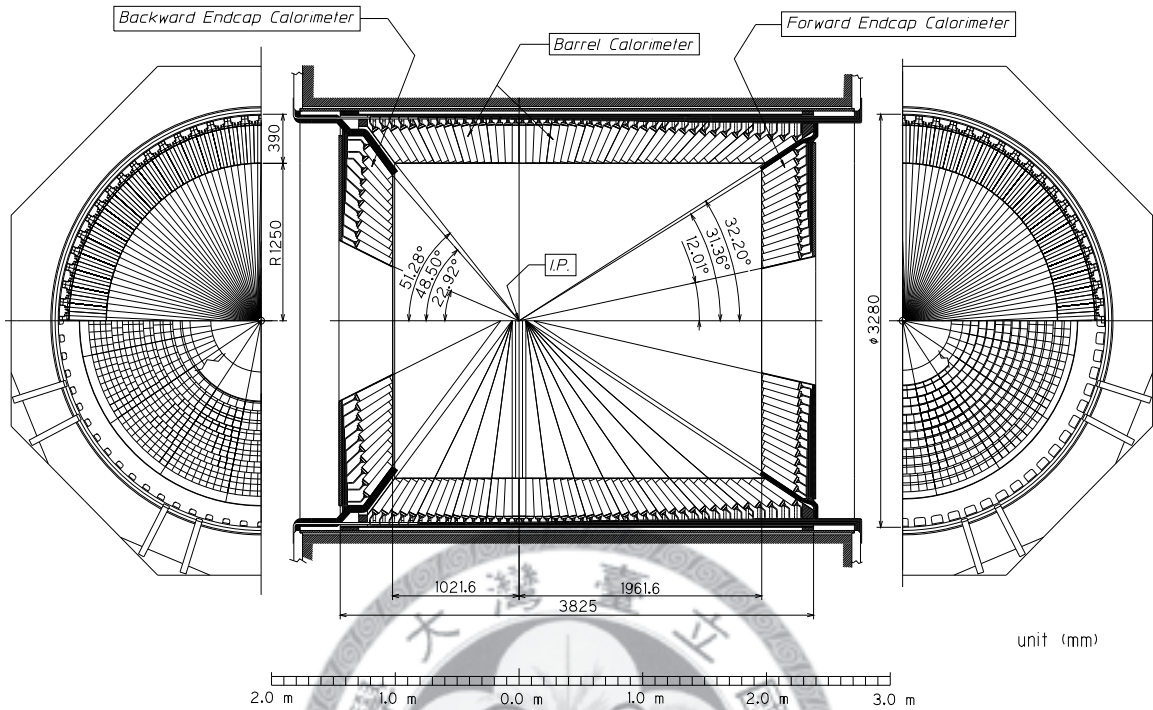
Figure 2.12: The overall configuration of the electromagnetic calorimeter. The unit of the figure is in mm.

2.10 K_L and Muon Detector (KLM)

The mainly purpose of the KLM is to detect the neutral kaons (K_L^0) and muons ($\mu^\pm$) with momenta greater than 600 MeV/c. The KLM detector consists of 15 (14) layers of glass-electrode-resistive plate counters (RPCs) and 14 (14) layers of 4.7 cm-thick iron plates arranged alternately in the barrel (end-cap) region. It covers the region from 17° to 155°. The illustration of KLM is shown in Fig. 2.13. A shower of ionizing particles is generated if a K_L interacts with the iron plates. The location of the shower provides the direction of K_L. The KLM hit associated charged tracks will be identified as muons.

RPCs consists of two parallel resistive plates with gas-filled gap, which provides a high resistivity. An ionized particle passing through the gap induces a streamer in the gas, and results a local discharge of the plates. The discharge generates a signal, and the location

and time are recorded. Figure 2.14 shows the arrangement for RPCs.
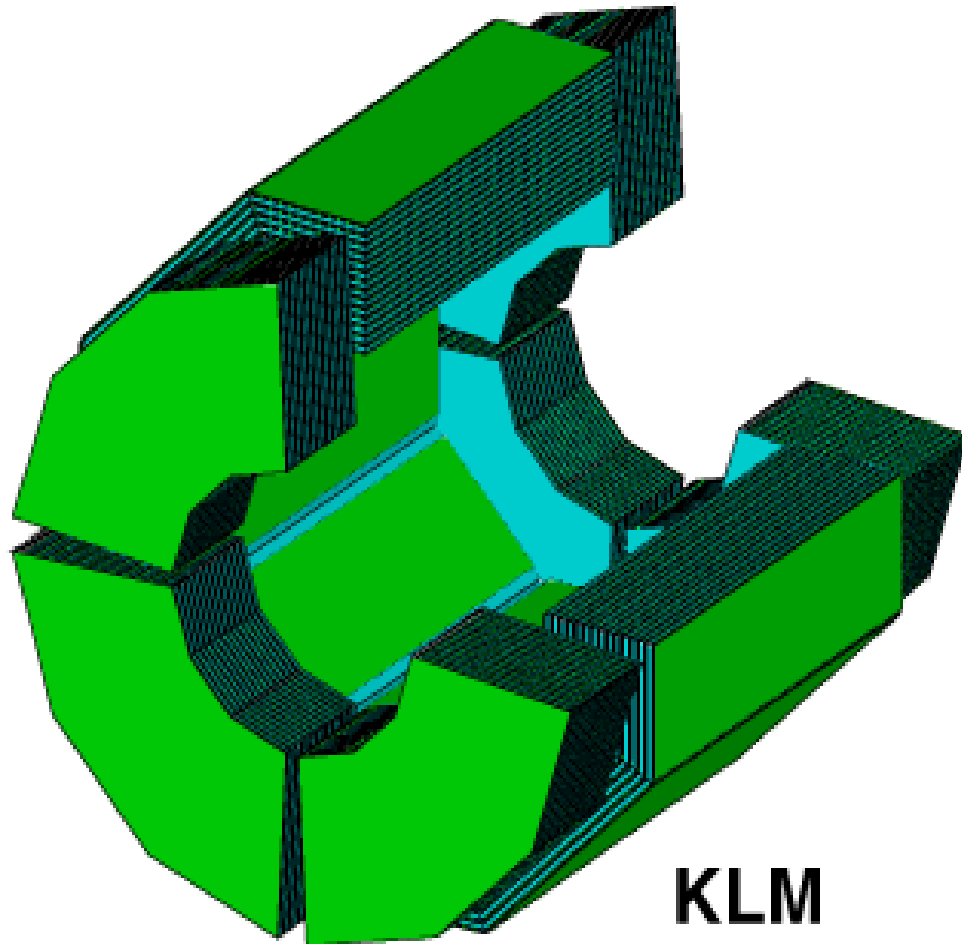
Figure 2.13: An illustration of KLM sub-detector.
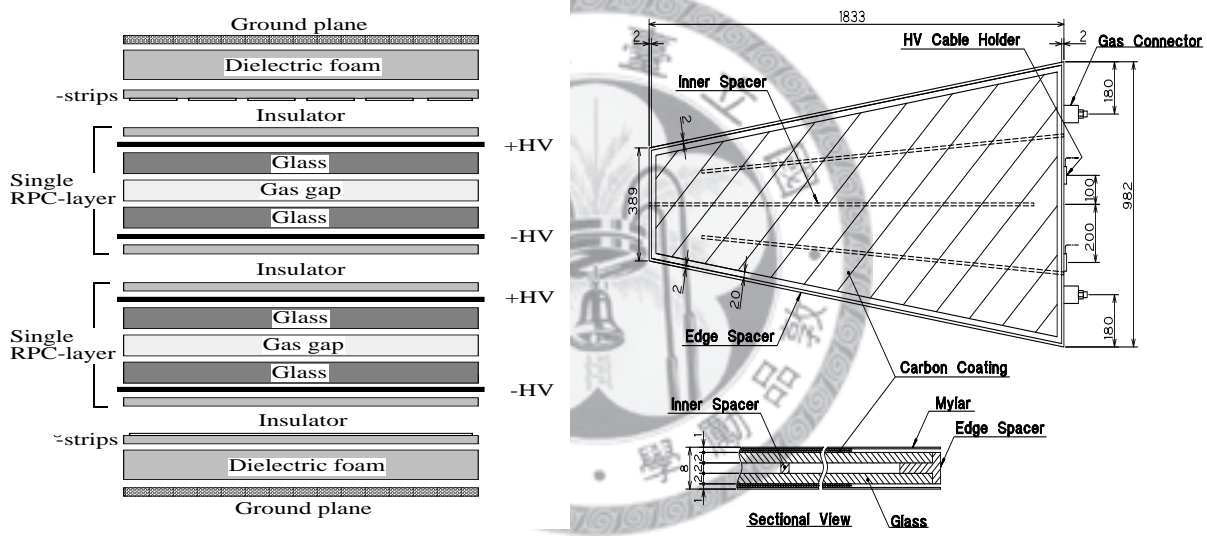
Figure 2.14: Schematic diagrams of the internal spacer arrangement for barrel (left) and endcap (right) RPCs.

Chapter 3

Analysis Method

3.1 Data Sample

This analysis is based on the data collected by the BELLE detector at the KEKB collider with asymmetric energy of e^+e^- (3.5GeV on 8GeV) at the $\Upsilon(4S)$ resonance. The data sample used is from Exp.7 to Exp.55, namely Case A data set, with 656.725 ± 8.940 million $B\overline{B}$ pairs.

We use EvtGen [20] to generate signal MC events, and we generated 2.624 million $B\overline{B}$ pair. The signal MC events are distributed into several groups from Exp.7 to Exp.55 according to the proportion of these experiments in the data sample and simulated with corresponding experiment condition by GEANT [21]. For the background study, we consider the Generic$B$ ($b \to c$ transition), Rare$B$ ($b \to$ non$c$), continuum ($e^+e^- \to q\bar{q}$, $q = u, d, s$ and c) and Taupair ($e^+e^- \to \tau^+\tau^-$) events. The background MCs are also generated and simulated by EvtGen and GEANT packages.

3.2 Particle Identification

3.2.1 K/π Identification

The K/π identification is based on dE/dx measurement by the CDC, TOF measurement and the measurement of the number of photoelectrons in the ACC. Each sub-detector provides a separation yield for different particle types in different momentum regions, as shown in Fig 3.1. The three information, which are almost independent, can be combined to form a likelihood ratio: $L_{xy} \equiv P_x/(P_x + P_y)$, where x and y denote the particle type: e, μ, π, K and p. For example, the charged tracks with $P_K/(P_\pi + P_K) > 0.6$ are regards as kaons and $P_K/(P_\pi + P_K) < 0.4$ as pions
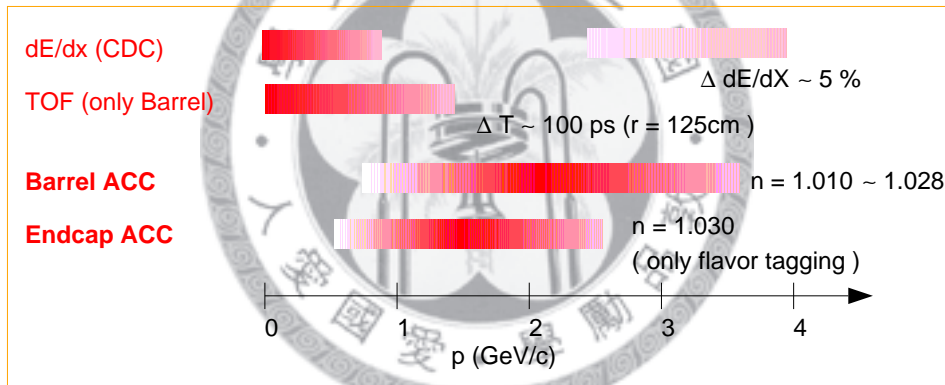
Figure 3.1: The momentum coverage of CDC, TOF and ACC.

3.2.2 Electron Identification

The electron identification is achieved by the following discriminants [22]:

- The ratio of energy deposited in ECL and the momentum of charged track measured by CDC.

- Shower shape at ECL.

- The matching between a cluster at ECL and charged track position extrapolated to ECL.

- The dE/dx measured by CDC.

- Light yield in ACC.

- Time-of-flight measured by TOF.

3.2.3   Muon Identification

The muon is identified by two information:

- Tracking information from CDC.

- Hits in the cluster at KLM.

However, the muon does not reach KLM if its momentum is below 500 MeV/c. The difference between the measured and expected range of a track allows us to assign a likelihood function of being a muon [23].

3.2.4 K_L Identification

The K_L candidates are selected by the following methods [24]:

- KLM clusters are made by combining the nearby hits which are with 5° opening angles.

- KLM clusters are classified as neutral or charged. To check if a KLM cluster is associated with charged tracks, each charged track is extrapolated to the first layer of KLM, and the meeting point is joined to IP by a straight line. If this condition

is satisfied the track is said to be associated with the KLM cluster. If this condition is not satisfied, KLM cluster is a neutral cluster.

- K_L candidates are required to satisfy the following two conditions:

  - Number of RPC superlayers in the KLM cluster ≥ 2 in the case of no associated ECL shower, and ≥ 1 when it has an associated ECL shower.

  - There should not be any associated charged track with KLM cluster.

The information of K_L candidates are stored in a table called **MDST_Klong**.

3.3   Full Reconstructed Tagging Method

In order to confirm the signal events are from $B\overline{B}$ decays, one of the B mesons in the events are reconstructed in the selected hadronic decay modes. We use the full-recon package in the belle library to reconstruct the hadronic B meson which is called B_{tag}. The B_{tag} candidates are rebuilt by a pair of mesons each with a positive and a negative sign. In the case of B^0, the plus charge meson is required to come from one of π^+, ρ^+, a_1^+, or $D_s^{(*)+}$ candidates, while the minus charge meson should be D^- or D^{*-}. For $\overline{B^0}$ candidates, the charges should have a flipped sign. The selected decay channels are listed in Table 3.1. The selection of B_{tag} candidates is based on two kinematic variables, beam-constraint mass (M_{bc}) and energy difference (ΔE). The definitions of these two variables are in the following equations.

$$M_{\mathrm{bc}} = \sqrt{E_{beam}^2 - p_B^2}, \tag{3.1}$$

$$\Delta E = E_B - E_{beam}, \tag{3.2}$$

where E_{beam} is the beam energy in the e^+e^- center-of-mass (CM) frame, and p_B and E_B are the reconstructed momentum and energy of the B_{tag} in CM frame. If there are more than one B_{tag} candidate found, the reduced χ^2 which is provided by the full-recon

module, which is based on ΔE, M_D and $M_{D^*} - M_D$, will be used to choose the best B_{tag} candidate.

Table 3.1: The selected mode of hadronic tagging method

Particle	Decay Mode
B^0	$D^{(*)-}\pi^+$
	$D^{(*)-}\rho^+$
	$D^{(*)-}a_1^+$
	$D^{(*)-}D_s^{(*)+}$
D^{*-}	$\overline{D^0}\pi^-$, $D^-\pi^0$
D_s^{*+}	$D_s^+\gamma$
D^0	$K^-\pi^+$, $K_s\pi^0$, K^+K^-
	$K^-\pi^+\pi^0$, $K_s\pi^+\pi^-$
	$K^-\pi^+\pi^+\pi^-$
	$K_s\pi^+\pi^-\pi^0$
D^-	$K^+\pi^-\pi^-$, $K^+\pi^-\pi^-\pi^0$
	$K^+K^-\pi^-$, $K_s\pi^-$
	$K_s\pi^-\pi^0$
	$K_s\pi^-\pi^-\pi^+$
D_s	$K_s\pi^+$, $K^+K^-\pi^+$
	$K^+\pi^-\pi^+$
a_1^-	$\rho^0\pi^-$
ρ^0, ρ^-	$\pi^+\pi^-$, $\pi^-\pi^0$

3.4   Event Selection

After the best B_{tag} described in the previous section is decided, the signal box for B_{tag}, and quality cuts of particles are required. Then, no additional background particles, such as charged particles, π^0 and K_L, should exist in the same event after removing the daughter product of B_{tag}. The M_{bc}, ΔE, and charge sign requirements of B_{tag} are included in the selection of signal box. There is an additional lepton identification cut for the daughter particles B_{tag} to reject the events with B_{tag} decays into leptons.

The following is a summary of final selection criteria:

- **B_{tag} selections**

  The B_{tag} candidates are required to match 5.27 GeV/c^2 < M_{bc} < 5.29 GeV/c^2 and
  -0.08 GeV < ΔE < 0.06 GeV. In the following study, we will use the B_{tag} sideband
  region to check the agreement between the data and MC output. The B_{tag} sideband
  region is defined 5.20 GeV/c^2 < M_{bc} < 5.25 GeV/c^2 with ΔE within ± 0.3 GeV. In
  both signal and B_{tag} sideband region, the B_{tag} should be neutral.

- **π^0 selections**

  A π^0 candidate is reconstructed from two photons with energy larger than 50 MeV.
  The invariant mass of the photon pair should be between 115 MeV/c^2 and 152
  MeV/c^2, and the energy asymmetry of π^0 candidates should be less than 0.9.

- **Track selection**

  An additional track particle candidate is a redundant charged particle with trans-
  verse momentum greater than 0.1 GeV/c in the event after forming a B_{tag}.

- **K_L selections**

  A K_L candidate is selected from **MDST_Klong** table with hits on more than two
  layers in the KLM cluster.

- **Track, π^0, K_L vetoes**

  No additional tracks, π^0 and K_L are required to remain in the event after removing
  the decay products of B_{tag}. The distribution of N_{track} and N_{π^0} are shown in Fig. 3.2.

- **Lepton veto for B_{tag}**

  The lepton veto is the only particle veto, which is not for the extra particles in
  the entire events, but for the daughter particles of B_{tag}. There is no electron or
  μ identified requirement for the reconstructed particles in the frecon module, so
  electrons or μ might be misidentified as π or K meson. Here the daughters of B_{tag}
  are required that their eid < 0.9 and μid < 0.9 to avoid fake π or K. This veto
  application rejects 50% events from tau pair sample and keeps 93% signal events.

- **cos θ_B**

  The $\cos \theta_B$ is defined as the cosine value of the angle of B flight direction with respect to the beam direction in the center-of-mass frame of $\Upsilon(4S)$. All reconstructed events must be within the requirement of $-0.9 < \cos \theta_B < 0.9$. Distributions of $\cos \theta_B$ in MC and data are different near ± 1 for $\cos \theta_B$ distribution(Fig. 3.3). To avoid those events around ± 1, we apply the $\cos \theta_B$ cut for both B_{tag} M_{bc} sideband and signal regions. The shape of $\cos \theta_B$ are shown in Fig. 4.5.

- **cos θ_T**

  The definition of θ_T is the angle of the B_{tag} thrust axis with respect to the beam axis in the CM frame, the distribution is shown in Fig. 3.4. To suppress the continuum background, the absolute value of $\cos \theta_T$ is required to be less than 0.6. This selection can reject 60% continuum events yet remain 80% signal events.

- **E_{ECL} calculation**

  E_{ECL} is the sum of all remaining energies of the cluster in ECL which are not associated with B_{tag} daughter particles. Different energy thresholds are applied in different part of ECL.

    - $E_{cluster} > 0.05$ GeV (barrel),

    - $E_{cluster} > 0.10$ GeV (forward end-cap),

    - $E_{cluster} > 0.15$ GeV (backward end-cap).

  The E_{ECL} variable is the most powerful one to separate signal and background events. For the signal events, the E_{ECL} distribution peaks at low energy since the contribution of ECL cluster almost comes from the beam background. The study of threshold energy will be presented in Appendix A. It will be used as the PDF to extract the signal events, and the E_{ECL} distributions for different samples are shown in Fig 4.4.
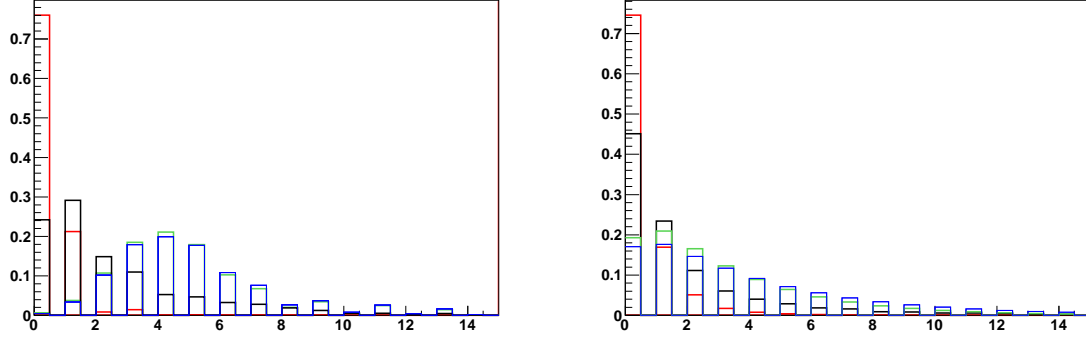
Figure 3.2: The N_{track}(left) and N_{π^0}(right) distribution of signal and backgrounds. The red one denote the signal, the others are backgrounds.
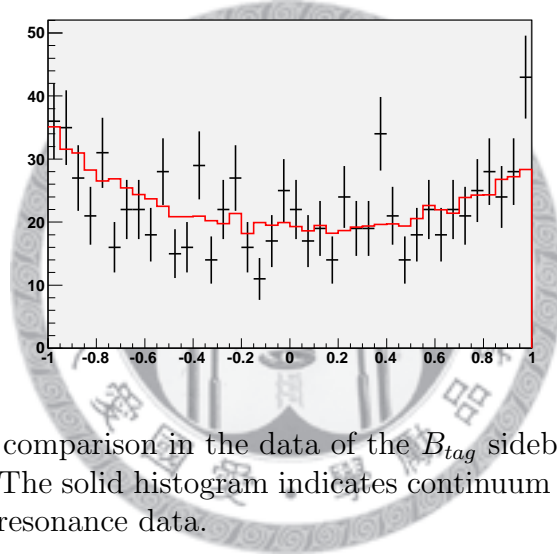
Figure 3.3: The $\cos\theta_B$ comparison in the data of the B_{tag} sideband. In this plot, we did not use the $\cos\theta_T$ cut. The solid histogram indicates continuum MC, and the points with error bar indicated off-resonance data.

The signal events will be extracted in the signal box, and the event selection for the signal box in this analysis are listed in Table 3.2. Moreover, the discussion of PDF construction in later chapter.

3.4.1 The Definition of $\cos\theta_T$

In this analysis, the dominant background comes from continuum events. We defined a new variable $\cos\theta_T$ to suppress continuum background. This variable is the angle of B_{tag} thrust axis corresponding to the beam axis. The $\cos\theta_T$ shapes are different in signal and continuum events. In signal MC, the shape of $\cos\theta_T$ is like a parabola; in continuum
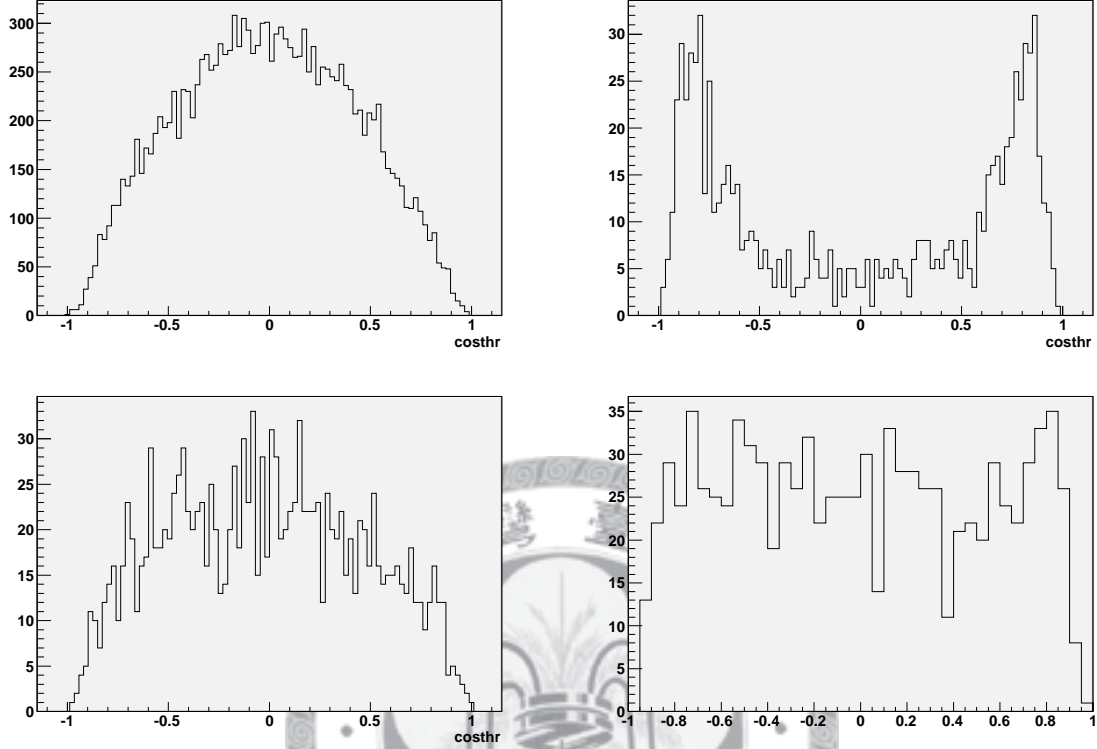
Figure 3.4: The $\cos\theta_T$ distribution for signal, continuum, GenericB MC and tau-pair MC(from left to right, top to bottom). The signal shape is similar to GenericB MC, like parabola, yet not similar in non-B background.

Table 3.2: Summary table of event selection.

	Signal box	B_{tag} $M_{\rm bc}$ sideband
B_{tag} selection	Neutral B	
	$5.27 < M_{\rm bc} < 5.29$ GeV/c^2	$5.2 < M_{\rm bc} < 5.25$ GeV/c^2
	$-0.08 < \Delta E < 0.06$ GeV	$-0.1 < \Delta E < 0.1$ GeV
	$|\cos\theta_B| < 0.9$	
	$|\cos\theta_T| < 0.6$	-
	No tag-side lepton	
B_{sig} selection	No signal-side track and π^0	
	No signal-side K_L	
	$E_{ECL} < 1.2$ GeV	

Figure 3.5: The horizontal axis is $\cos\theta_B$, and the perpendicular axis is $\cos\theta_T$. The events accumulate in left-top and right-bottom parts.

events, there are two peaks at around ± 0.85.

At first, we thought this new variable might be used as PDF in the fitter. Yet we found $\cos\theta_B$ and $\cos\theta_T$ are correlative in the continuum MC(Fig. 3.5). The distribution of $\cos\theta_B$ in continuum MC changed with different $\cos\theta_T$(Fig. 3.6). Although the correlation is not significant in signal MC(Fig. 3.7), the shape of $\cos\theta_B$ also changed with different $\cos\theta_T$(Fig. 3.8). Because of the limited statistics of MC and the correlation of these two variables, constructing a 2-D PDF and combining two variables via Fisher discriminant are not good choices. Therefore we apply a symmetric $\cos\theta_T$ criterion, $|\cos\theta_T| < 0.6$. This selection can reject 60% continuum events yet remain 80% signal events.

3.5 Estimation of background

We estimated the signal and background from Monte-Carlo simulation and off-resonance data. The background considered are Generic $B\overline{B}$ decays, Rare B decays, continuum events($e^+e^- \to u\overline{u}, d\overline{d}, s\overline{s}, c\overline{c}$) and Tau-pair events($e^+e^- \to \tau^-\tau^+$). The events are scaled to the equivalent luminosity of data. Table 3.3 shows the expected backgrounds in the signal box and the expected E_{ECL} distribution on data is shown in Fig.3.9. All backgrounds are estimated from MC but Non-B background. The Non-B background includes con-
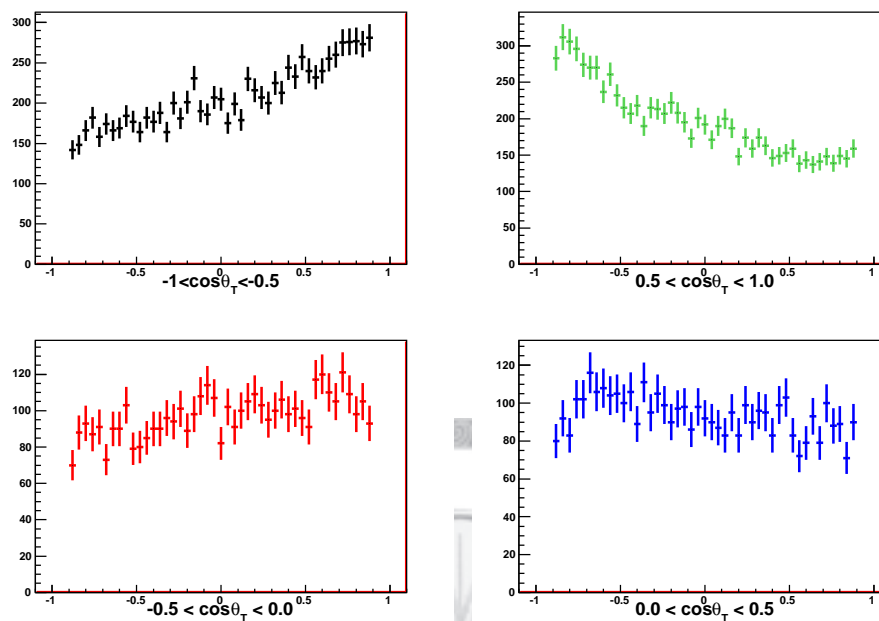
Figure 3.6: The $\cos\theta_B$ distributions change for different $\cos\theta_T$ region in continuum MC.
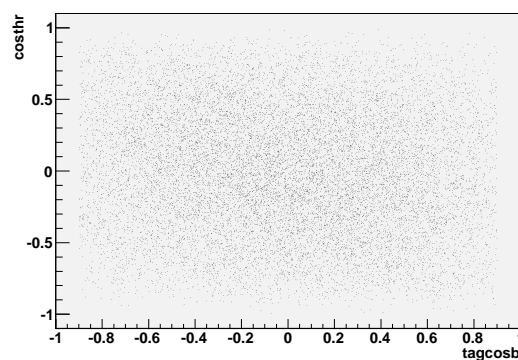
Figure 3.7: The horizontal axis is $\cos\theta_B$, and the perpendicular axis is $\cos\theta_T$. The correlation is not clear in the signal MC yet the shape of $\cos\theta_B$ would have apparent difference.
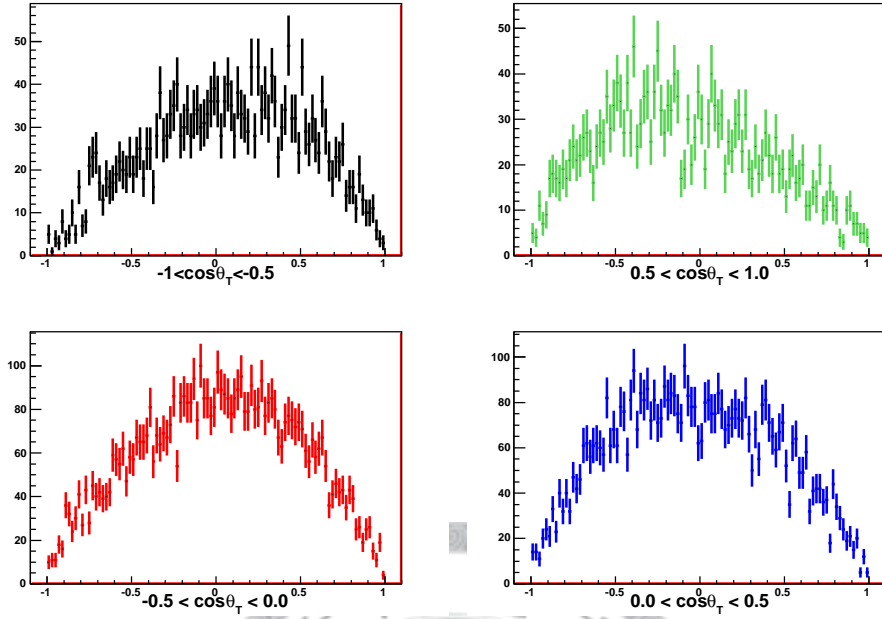
Figure 3.8: The $\cos\theta_B$ distributions change for different $\cos\theta_T$ region in the signal MC.

tinuum and tau pair events, and the expected number in signal box is obtained from off-resonance data. Consider the less events of off-resonance data in signal box, we use the events without $\cos\theta_T$ requirement and the efficiency of $\cos\theta_T$ to calculate the expected events in the signal box. The comparison of $\cos\theta_T$ for off-resonance data and continuum MC are shown in Fig. 3.10.

Table 3.3: Estimation of background in signal box.

Mode	
Non-B	64 ± 16
$B\overline{B}$	67.3 ± 2.6
rare B	3.7 ± 0.3
Total	136.6 ± 16.2
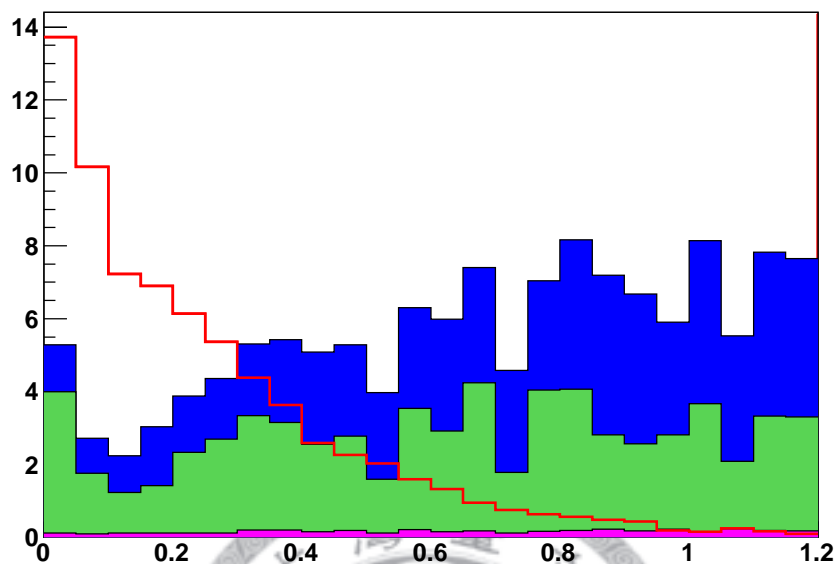
Figure 3.9: The expected E_{ECL} distribution on data. The blue part denotes Generic$B$, green one for Non-B, purple one for Rare$B$ and the red line is signal(500 times).
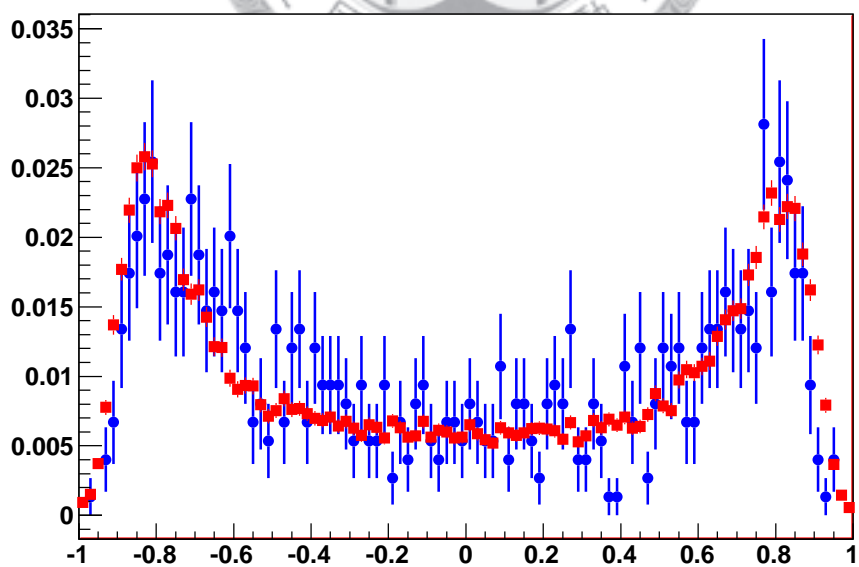
Figure 3.10: The Comparison of $\cos\theta_T$ in off-resonance data and continuum MC. The red point indicates the continuum MC, and the blue point is for off-resonance data.

3.6   Control Sample Study

Although Monte-Carlo simulation provides a good way to model the signal and background events, there are still some difference between data and MC. Consequently, we need a control sample to study the discrepancy in these two outputs.

Double-tagged samples are used as the control samples in this analysis where one B is fully reconstructed by the hadronic decays mentioned in the previous chapter, and the other one is from one of control samples.

Considering the fraction of the events pass through fullrec-tagged module is very low(Table 3.4), we should choose the decay channels with higher branching fraction, i.e. $B^0 \rightarrow D^{*-}l^+\nu$ and $B^0 \rightarrow D^-l^+\nu$, to check if the branching fraction measured by fitting the E_{ECL} distribution matches the PDG value. In this chapter, all the control sample study is based on $605fb^{-1}$ data.

The D or D^* decays in the control samples are:

- D^{*+} decay: $D^0\ \pi^+$,

- D^0 decay: $K^-\ \pi^+$

- D^+ decay: $K_s\ \pi^+$, $K^-\pi^+\pi^+$.

The event selections are listed in Table 3.5.

In Table 3.5, MM^2 is the square of the missing mass, and Δm is the difference of the invariant mass of D^* candidate and D candidate. The definitions of these two variables are:

$$MM^2 = (P_{beam} - P_{B_{tag}} - P_{D^{(*)}l})^2 \tag{3.3}$$

Table 3.4: The fraction of the events pass through fullrec in different MC sample. The values is measured before applying any selection on B_{tag}. This fraction includes the effect of the fix_mdst module.

Mode	The fraction of events pass through fullrec module(%)
$B^0 \to D^{(*)\mp}\mu^{\pm}\nu$	5.0
$B^0 \to$ invisible final state	0.13

Table 3.5: The selection criteria for control samples

Decay mode	$B^0 \to D^{*-}\mu^+\nu$	$B^0 \to D^{*-}e^+\nu$	$B^0 \to D^-\mu^+\nu$	$B^0 \to D^-e^+\nu$
M_D	$1.8 < M_{D^0} < 1.9$		$1.84 < M_{D^\pm} < 1.9$	
Δm	$0.142 < \Delta m < 0.149$		-	
Missing mass square	$|MM^2| < 0.2$	$|MM^2| < 0.4$	$|MM^2| < 0.5$	$-1 < MM^2 < 2$

$$\Delta m = M_{D^*(K\pi\pi)} - M_{D(K\pi)}, \tag{3.4}$$

where P_{beam}, $P_{B_{tag}}$ and $P_{D^{(*)}l}$ are the four-momentum of the e^+e^- beam, B_{tag} and $B_{sig}(D^{(*)}+ l)$. The distribution for M_D, Δm and MM^2 for signal MC in each modes are shown in Fig. 3.11.

The reconstructed E_{ECL} distributions for the control samples are shown in Figure 3.12. Since the purity of the double-tagged events are good, the survived background events from MC is almost zero(In $B^0 \to D^*\mu\nu$ sample, the number of background is only 0.04 ± 0.06 events in the signal box, as shown in Fig. 3.13). The signal MC(of control samples) and data distribution are reasonably consistent. The branching fraction for these control samples agree with the PDG values(Table 3.6). According to the consistency, it is legitimate to use the E_{ECL} shape for the signal extraction.

Furthermore, the discrepancy of E_{ECL} distribution in each vetoes(track and π^0, lepton and K_L) would be used to study the corrected factor for the MC efficiency.

Table 3.6: The fitting result for the control samples.

	Yield	measured result($\times 10^{-3}$)	PDG value
$B^0 \to D^{*\mp}\mu^{\pm}\nu$	50 ± 7.1	1.41 ± 0.20	1.38 ± 0.06
$B^0 \to D^{*\mp}e^{\pm}\nu$	84 ± 9.3	1.62 ± 0.18	1.38 ± 0.06
$B^0 \to D^{\mp}(D \to K_s\pi)\mu^{\pm}\nu$	9 ± 3.0	1.89 ± 0.63	2.23 ± 0.14
$B^0 \to D^{\mp}(D \to K_s\pi)e^{\pm}\nu$	20 ± 4.4	2.07 ± 0.46	2.23 ± 0.14
$B^0 \to D^{\mp}(D \to K\pi\pi)\mu^{\pm}\nu$	90 ± 9.5	1.99 ± 0.21	2.04 ± 0.01
$B^0 \to D^{\mp}(D \to K\pi\pi)e^{\pm}\nu$	170 ± 12.3	1.93 ± 0.14	2.04 ± 0.01

3.7 Veto Studies

The final state products of the signal-side B meson cannot be detected by the BELLE detector, thus three vetoes(track, π^0, and K_L) are applied to reject extra particles from background events. However, the efficiency of vetoes is different between the data sample and the simulation sample. In this chapter, the study on the discrepancy is presented.

The veto efficiency from a data sample and the corresponding MC sample was measured in the events within $0 < E_{ECL} < 0.4$ GeV, and the double ratio of efficiency from the data sample to the MC output is calculated.

The efficiency in data and MC samples are defined as

$$\epsilon_{MC} = \frac{N_{MC} \text{ with veto}}{N_{MC} \text{ without veto}} \tag{3.5}$$

$$\epsilon_{data} = \frac{N_{data} \text{ with veto}}{N_{data} \text{ without veto}}, \tag{3.6}$$

and the double ratio between data and MC sample is given by

$$\text{Double ratio} = \frac{\epsilon_{data}}{\epsilon_{MC}}. \tag{3.7}$$

In the beginning of the efficiency study, the central shift plus 1σ statistical error would be quoted as the systematic error. However, the double ratio was found to be too large

to simply quote as systematic uncertainty. In the following section, we will study the correlation between the double ratio of efficiencies and the decay mode. The central shift part of the double ratio would be used to calibrate the MC efficiencies, and the statistic error is included into systematic uncertainty. The summary table of double ratio for each mode is shown in Table 3.7.

3.7.1 Tracks and π^0 veto

As mentioned in the previous chapter, there should be no extra charged particle or π^0 candidate in the signal event after removing the daughter products of the B_{tag}. The selection for additional track and π^0 are listed in Chapter 3.4. The track/π^0 veto efficiency are obtained by the events before and after the application of the vetoes in the $E_{ECL} < 4$ region. The track/π^0 veto efficiency are estimated to be $0.886 \pm 0.006/0.872 \pm 0.007$ for MC sample and $0.893 \pm 0.041/0.839 \pm 0.049$ for data of the $D^*\mu\nu$ mode. Thus the double ratio for the $D^*\mu\nu$ sample is $1.008\pm0.047/0.962\pm0.057$. If we just simply quote the double ratio as a systematic uncertainty, there are 5.5% and 9.5% systematic uncertainties for track and π^0 veto. Yet comparing the double ratio of $D^*\mu\nu$ to the results in $D^*e\nu(1.015\pm 0.032/0.962\pm0.057),De\nu(0.992\pm0.018$ for $K\pi\pi$, 1.021 ± 0.040 for $K_S\pi)$ and $D\mu\nu(0.819\pm 0.023$ for $K\pi\pi$, 0.855 ± 0.111 for $K_S\pi)$, all of them are consistent within 1σ. Therefore, we believe the discrepancy of the track and π^0 veto is mode-independent. The average of the central shifts in the double ratios of each modes are as calibration factor for MC samples, and the average of statistical errors would be quoted as a systematics uncertainty from the efficiency of track and π^0 veto. The Fig. 3.16-3.19 show the comparison of the E_{ECL} distribution for track veto, and Fig. 3.20-3.23 are for π^0 veto.

The result of average mean shift for track veto is only -0.4% with a statistic error 1.2%. Thus we don't need to calibrate the efficiency of track veto, and then the central shift plus 1σ statistical error(1.6%) will be quoted as the systematic error for the track

veto.

For the π^0 veto, the average mean shift of -5.4% will be used for calibrating the efficiency, and a systematic error of 2.0%(average statistical error) is included in the main analysis.

3.7.2 K_L veto

The K_L veto is to eliminate any events which associated with K_L candidate, because there should not be any K_L in the decay products of B_{tag}. A K_L candidate is selected by the KLM hits with at least two layers.

The K_L identification in BELLE is not good enough. In previous study [24], there is a $20\% \sim 30\%$ discrepancy between the data sample and the MC output. Therefore, we check the associated systematics of K_L veto first. We emphasize it is impossible to have any real K_L neither in B_{tag} nor in signal-side B. After the application of K_L veto, the backgrounds from $GenericB$ MC are reduced 40% with 11% signal events loss.

In $D^*\mu\nu$ sample, the K_L efficiency is obtained to be $80.8 \pm 1.0\%$ in the MC and $95.0 \pm 3.4\%$ in the data sample. The double ratio between the data sample and the MC output is measured to be 1.176 ± 0.045. We also compare the double ratio with other modes(Table. 3.7), all results are consistent with each other in 2σ. Figure 3.24- 3.27 show the comparison between with and without K_L veto.

The suppressed background in B events are following modes.

- $B^0 \to Dl\nu$, $D \to K_L l\nu$

- $B^0 \to D^*l\nu$, $D^* \to D\pi^0$, $D \to K_L l\nu$

- $B^0 \to D\rho$, $D \to K_L l\nu$

Table 3.7: Summary of the double ratios of efficiency, the calibration factors and statistic errors.

Decay mode	Track	π^0	K_L
$D^*\mu\nu$	1.008 ± 0.047	0.962 ± 0.057	1.170 ± 0.043
$D^*e\nu$	1.015 ± 0.032	1.007 ± 0.042	1.108 ± 0.044
$D(K\pi\pi)e\nu$	0.992 ± 0.018	0.898 ± 0.034	1.075 ± 0.031
$D(K_s\pi)e\nu$	1.021 ± 0.040	0.910 ± 0.095	1.051 ± 0.101
$D(K\pi\pi)\mu\nu$	0.989 ± 0.023	0.819 ± 0.042	1.064 ± 0.040
$D(K_s\pi)\mu\nu$	0.855 ± 0.111	0.847 ± 0.133	-
Average calibration factor(%)	-0.4	-5.4	9.6
Average statistic error(%)	1.2	2.0	2.0
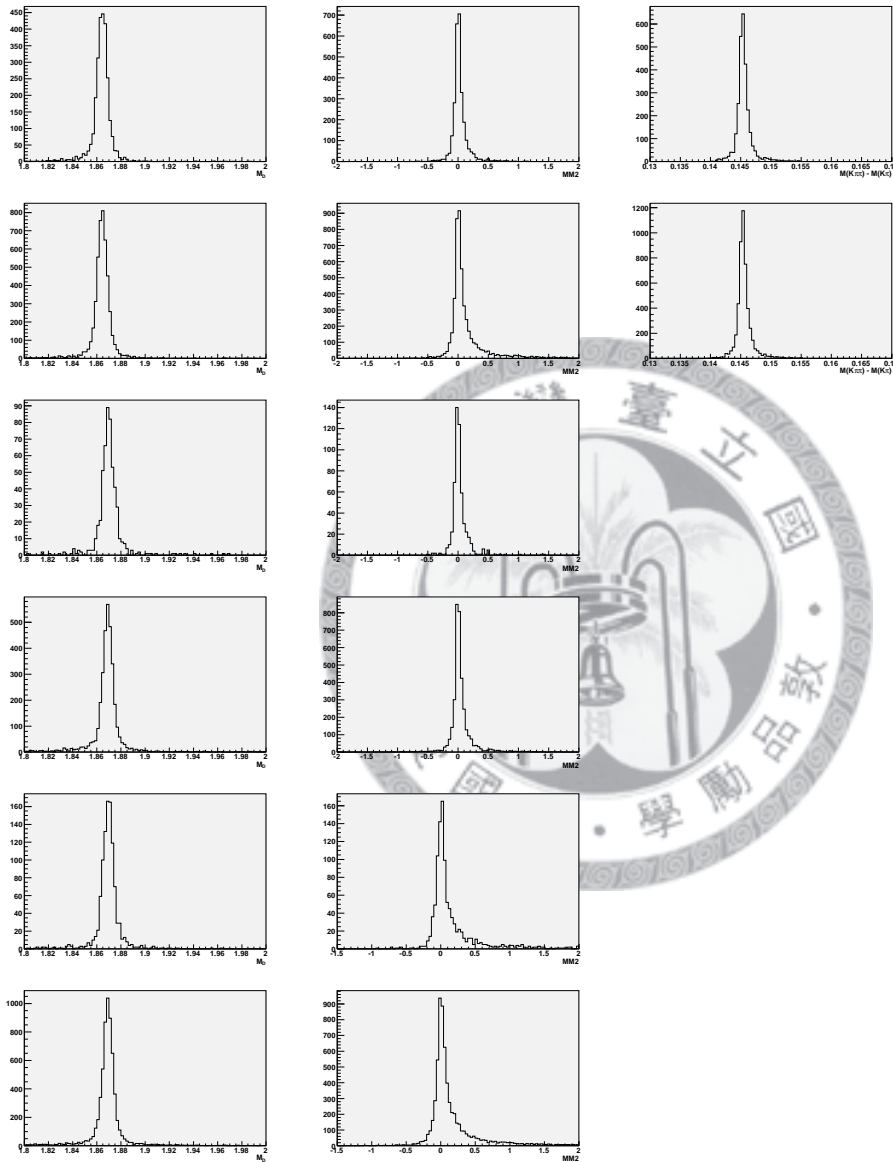
Figure 3.11: M_D, MM^2 and Δm distribution for signal MC in control samples. For top to bottom is $D^*\mu\nu$, $D^*e\nu$, $D(K\pi\pi)\mu\nu$, $D(K_s\pi)\mu\nu$, $D(K\pi\pi)e\nu$ and $D(K_s\pi)e\nu$.
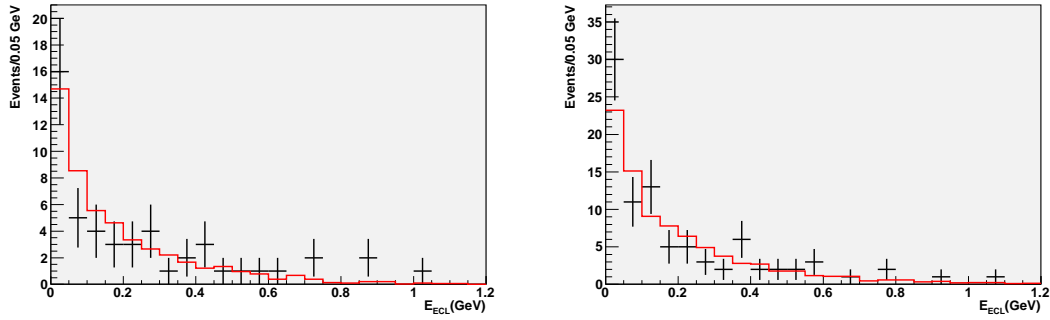
Figure 3.12: The E_{ECL} distribution for the fullrecon-tagged $B \to D^*l\nu$ candidates. The left-hand side plot is the muon mode, and the right-hand side is the electron mode. The red solid line indicates the MC prediction, and the point with error bar indicates the data.
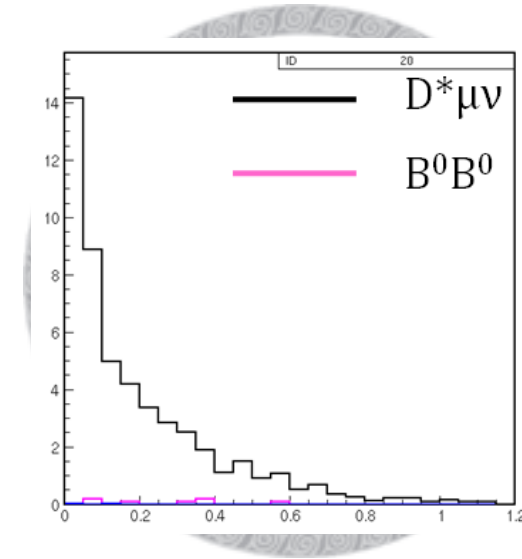
Figure 3.13: The expected E_{ECL} distribution for the fullrecon-tagged $B \to D^*l\nu$ candidates.
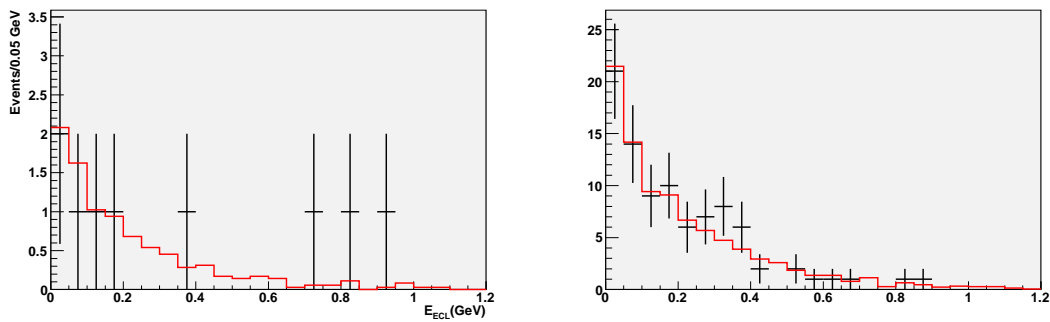
Figure 3.14: The E_{ECL} distribution for the fullrecon-tagged $B^0 \to D\mu\nu$ candidates. The left-hand side plot is for $D \to K_s\pi$, and the right-hand side is for $D \to K\pi\pi$.
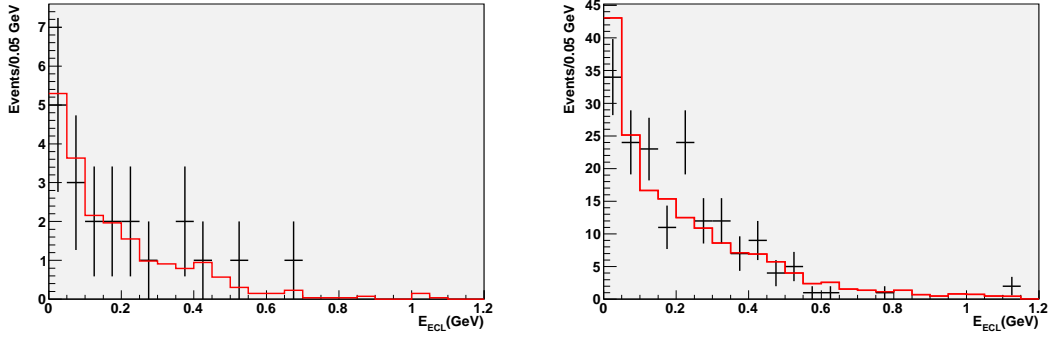
Figure 3.15: The E_{ECL} distribution for the fullrecon-tagged $B^0 \to De\nu$ candidates. The left-hand side plot is for $D \to K_s\pi$, and the right-hand side is for $D \to K\pi\pi$.
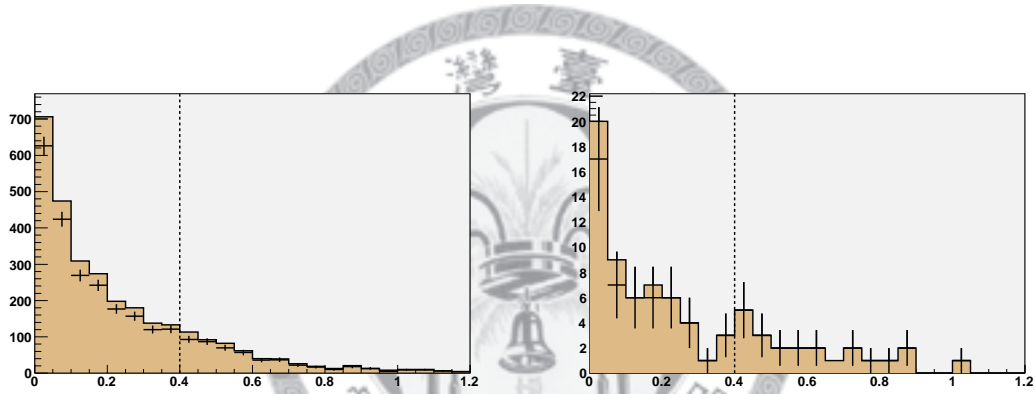
Figure 3.16: The E_{ECL} distributions from $D^*\mu\nu$ sample with and without the track veto. The events are rebuilt from MC output(left) and data sample(right). The colored histogram indicates the events before applying track veto, and the crossing dot is for the survived events after introducing veto selection.
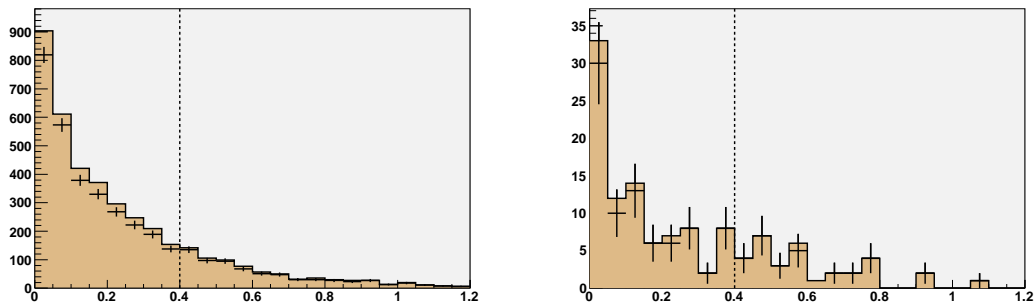
Figure 3.17: The E_{ECL} distributions from $D^*e\nu$ sample with and without the track veto. The events are rebuilt from MC output(left) and data sample(right).
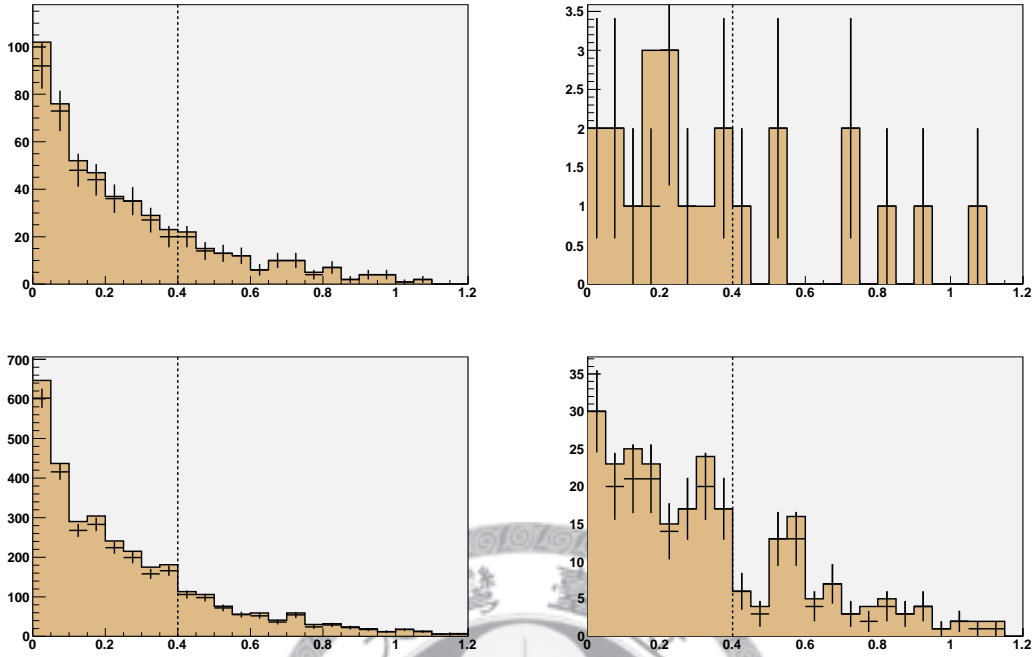
Figure 3.18: The E_{ECL} distributions from $D\mu\nu$ sample with and without the track veto. The events are rebuilt from MC(left) and real data(right). The upper plots are for sub-decay $D \to K_s\pi$, then the bottoms are for $D \to K\pi\pi$.
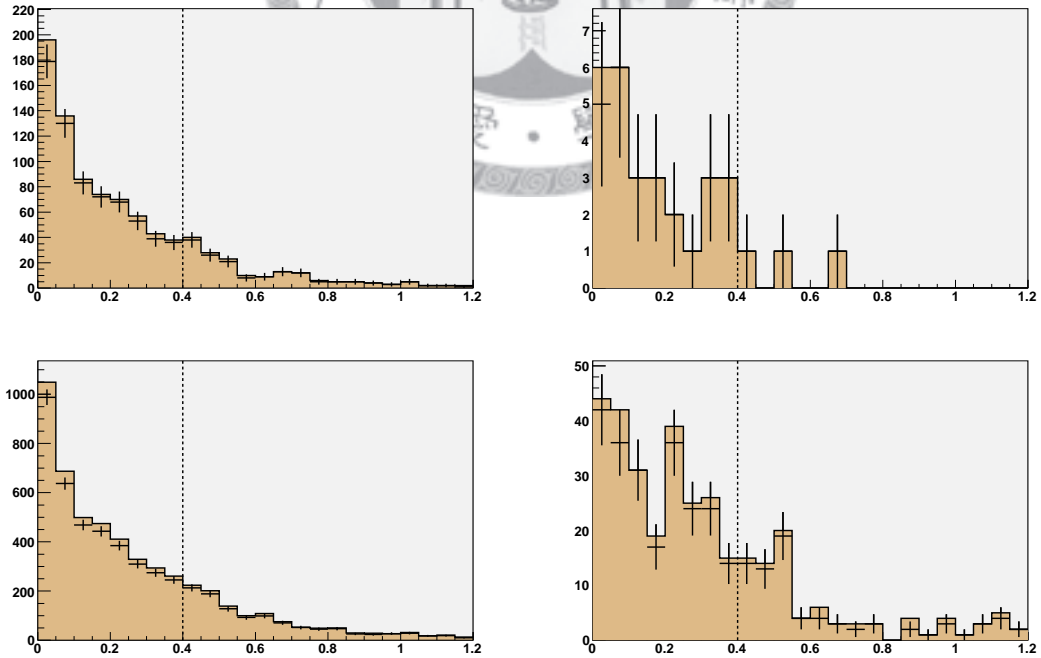
Figure 3.19: The E_{ECL} distributions from $De\nu$ sample with and without the track veto. The events are rebuilt from MC(left) and real data(right). The upper plots are for sub-decay $D \to K_s\pi$, then the bottoms are for $D \to K\pi\pi$.
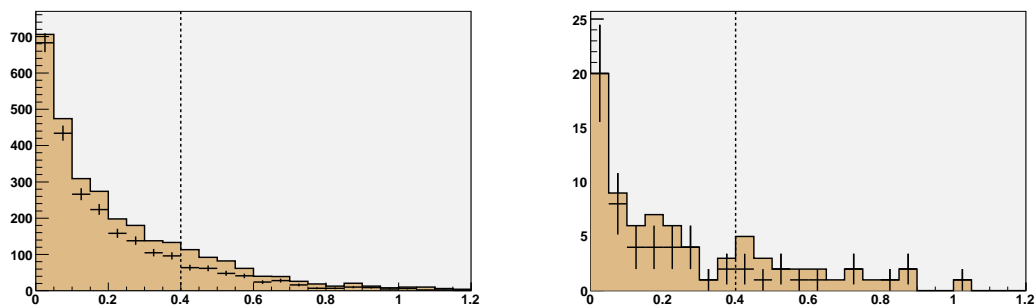
Figure 3.20: The E_{ECL} distributions from $D^*\mu\nu$ sample with and without the π^0 veto. The events are rebuilt from MC output(left) and data sample(right). The colored histogram indicates the events before applying π^0 veto, and the crossing dot is for the survived events after introducing veto selection.
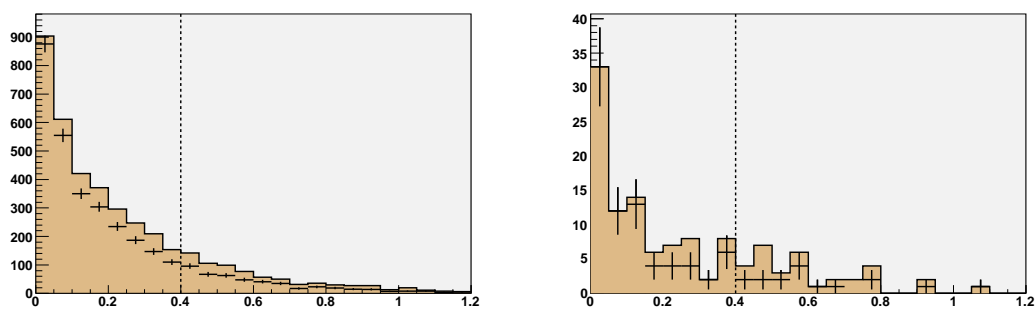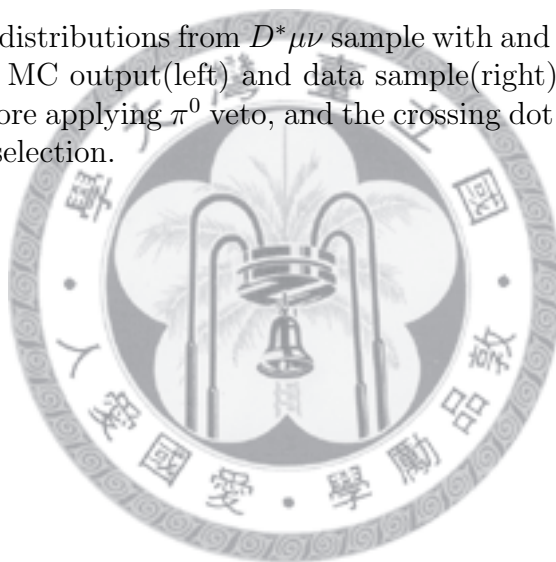
Figure 3.21: The E_{ECL} distributions from $D^*e\nu$ sample with and without the π^0 veto. The events are rebuilt from MC output(left) and data sample(right).
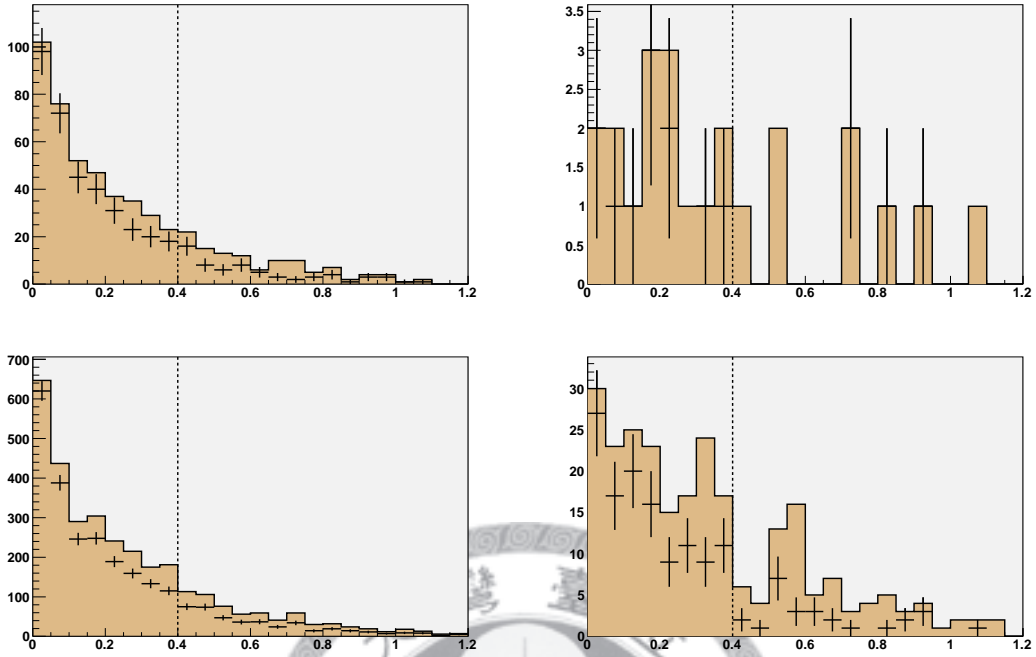
Figure 3.22: The E_{ECL} distributions from $D\mu\nu$ sample with and without the π^0 veto. The events are rebuilt from MC(left) and real data(right). The upper plots are for sub-decay $D \to K_s\pi$, then the bottoms are for $D \to K\pi\pi$.
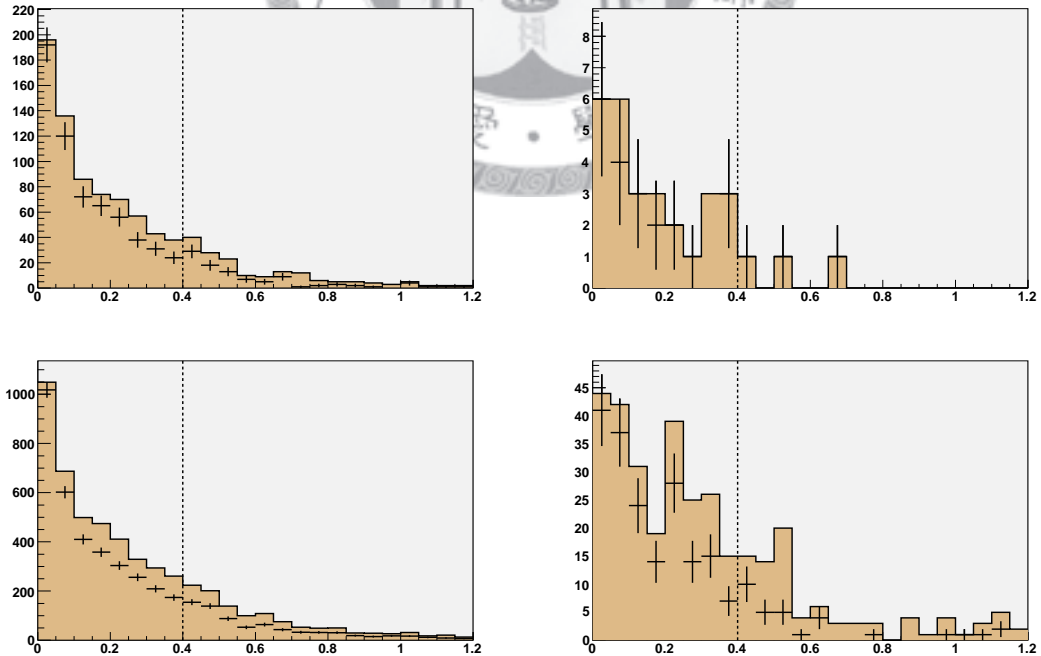
Figure 3.23: The E_{ECL} distributions from $De\nu$ sample with and without the π^0 veto. The events are rebuilt from MC(left) and real data(right). The upper plots are for sub-decay $D \to K_s\pi$, then the bottoms are for $D \to K\pi\pi$.
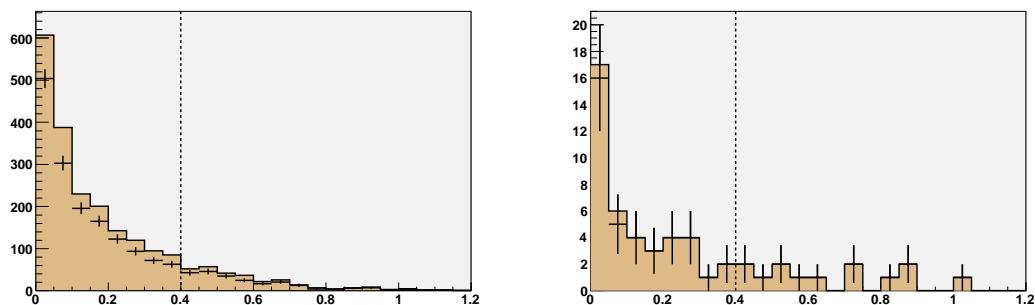
Figure 3.24: The E_{ECL} distributions from $D^*\mu\nu$ sample before and after the K_L veto. The events are rebuilt from MC output(left) and data sample(right). The colored histogram indicates the events before applying veto cut, and the corssing dot is for the survived events after introducing veto cut.
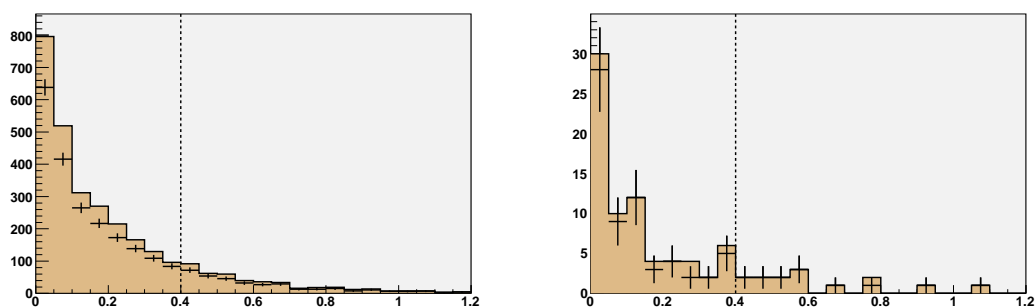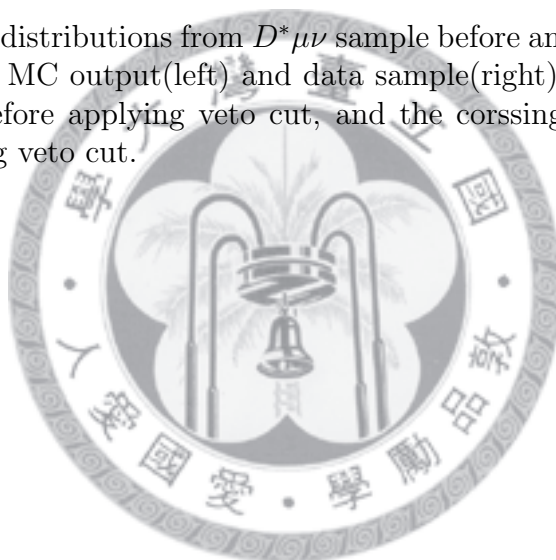
Figure 3.25: The E_{ECL} distributions from $D^*e\nu$ sample before and after the K_L veto. The events are rebuilt from MC(left) and real data(right).
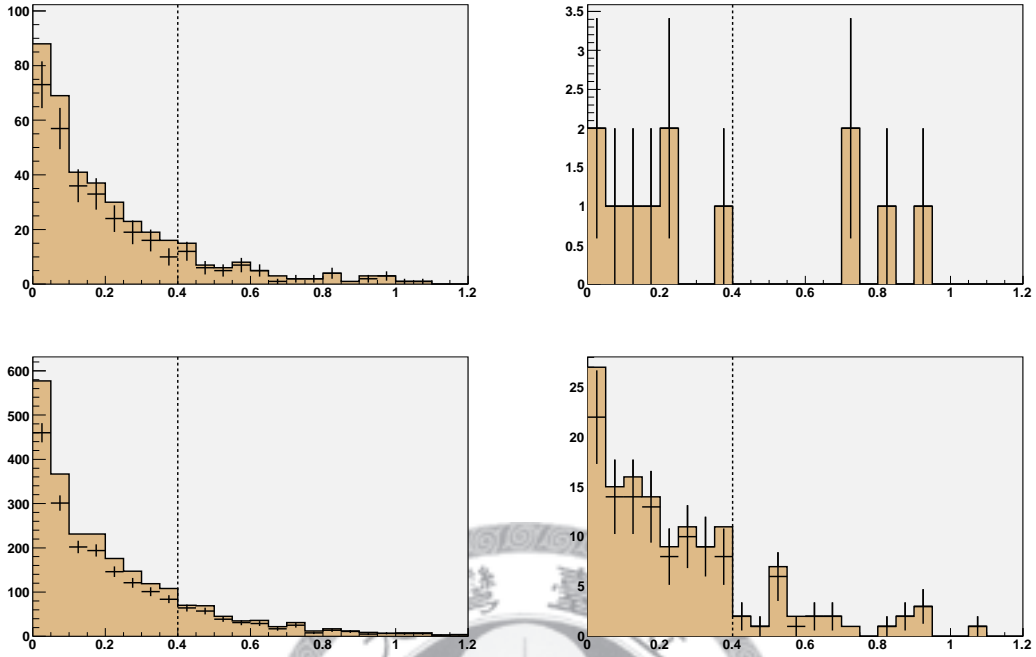
Figure 3.26: The E_{ECL} distributions from $D\mu\nu$ sample before and after the K_L veto. The events are rebuilt from MC(left) and real data(right). The upper plots are for sub-decay $D \to K_s\pi$, then the bottoms are for $D \to K\pi\pi$.
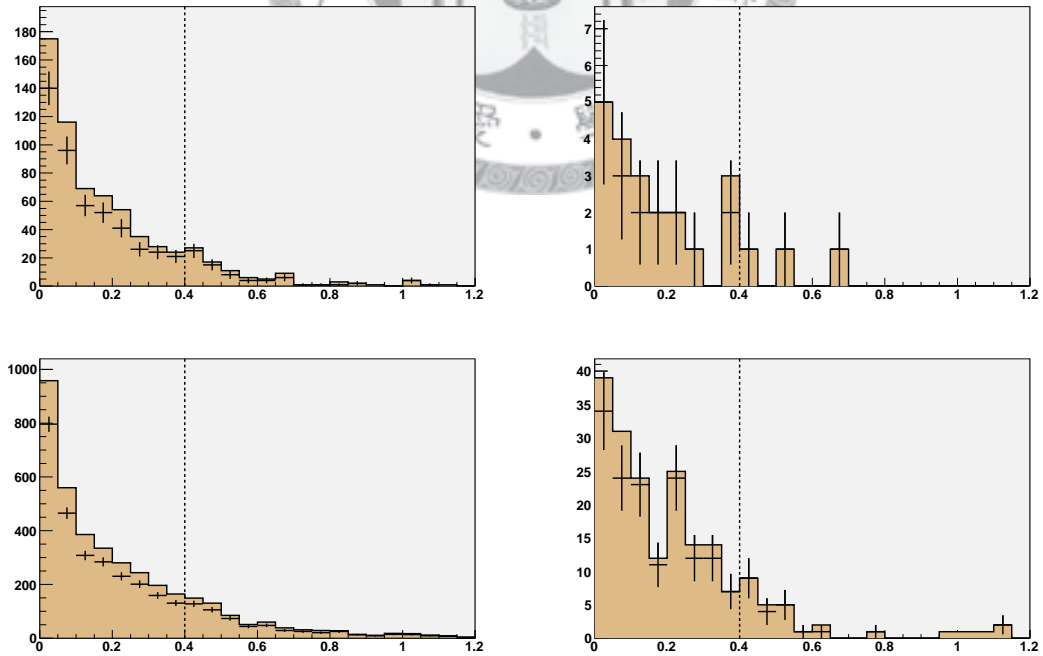
Figure 3.27: The E_{ECL} distributions from $De\nu$ sample before and after the K_L veto. The events are rebuilt from MC(left) and real data(right). The upper plots are for sub-decay $D \to K_s\pi$, then the bottoms are for $D \to K\pi\pi$.

Chapter 4

Extract Strategy and Result

We perform an unbinned extended likelihood fit that maximizes the likelihood function,

$$\mathcal{L} = \frac{e^{-\sum_j n_j}}{N!} \prod_{i=1}^{N} \left(\sum_j n_j P_j^i(E_{ECL}, \cos\theta_B) \right),$$ (4.1)

where i is the event identifier, j indicates one of the event type categories for signals and backgrounds, n_j denotes the yield of the j-th category, N is the number of events in fit, and P_j^i is the PDF for the j-th category.

In the final fit, three parameters are floated: the number of signal, Generic B and Non-B background events. The number of Rare B background is fixed to the expected value. All of the PDFs are fixed in the fit. The PDF construction and correlation study are presented in the following section.

4.1 PDF Construction for Fitting

With the 2D ML fit, we use histogram function to present the E_{ECL} distribution. Because we use the cluster energy threshold for E_{ECL} calculation, some data points accumulate only at $E_{ECL} = 0$ and there is no event between 0 and 0.05 GeV. We obtained the E_{ECL} PDFs with the events survived in the selection criteria listed in Table 3.2. The veto

of track and π^0 would affect on the E_{ECL} distribution but not the $\cos\theta_B$ distribution, as shown in Fig.4.1-4.2.

This property allows us to have significant $\cos\theta_B$ PDFs with higher statistic by using looser criteria of vetoes. But the distribution of $\cos\theta_B$ is correlated with $M_{\rm bc}$, the PDF of $\cos\theta_B$ should be obtained in the region of $5.27 < M_{\rm bc} < 5.29$ GeV. Figure 4.3 shows the distribution of $\cos\theta_B$ in the region of $5.2 < M_{\rm bc} < 5.25$ region. Here, we use Legendre polynomial to model the $\cos\theta_B$ distribution for each component in the fit. The selection of the PDF construction is listed in Table 4.1. All of the PDFs shown in Fig 4.4- 4.5 are obtained with corresponding MC samples, besides the E_{ECL} PDF for continuum background. Owing to the bad simulation on the E_{ECL} variable in continuum MC(Fig. 4.6), we use the E_{ECL} distribution from the off-resonance data instead. All the PDFs are summarized in Table 4.2.

Table 4.1: The selection criteria for E_{ECL} and $\cos\theta_B$.

E_{ECL}	$\cos\theta_B$
$5.2 < M_{\rm bc} < 5.29$	$5.27 < M_{\rm bc} < 5.29$
$-0.3 < \Delta E < 0.3$	$-0.08 < \Delta E < 0.06$
No tag-side lepton	
No signal-side track and π^0	N_{trk} and N_{π^0} are less than 3.
No signal-side K_L	N_{K_L} are less than 3.
$0 < E_{ECL} < 1.2$ GeV	

4.1.1 Correlation Check

In this section, we inspect whether the distributions of E_{ECL} and $\cos\theta_B$ are correlated or not. The distribution of $\cos\theta_B$ is checked in the different bins on E_{ECL}, and the plots are shown in Fig. 4.7- 4.10. Since the shapes of $\cos\theta_B$ would not change with different E_{ECL} bins, there is no correlation between E_{ECL} and $\cos\theta_B$. Therefore, The PDF($P_j^i(E_{ECL}, \cos\theta_B)$) can be simply presented as a product of the shapes in E_{ECL} and
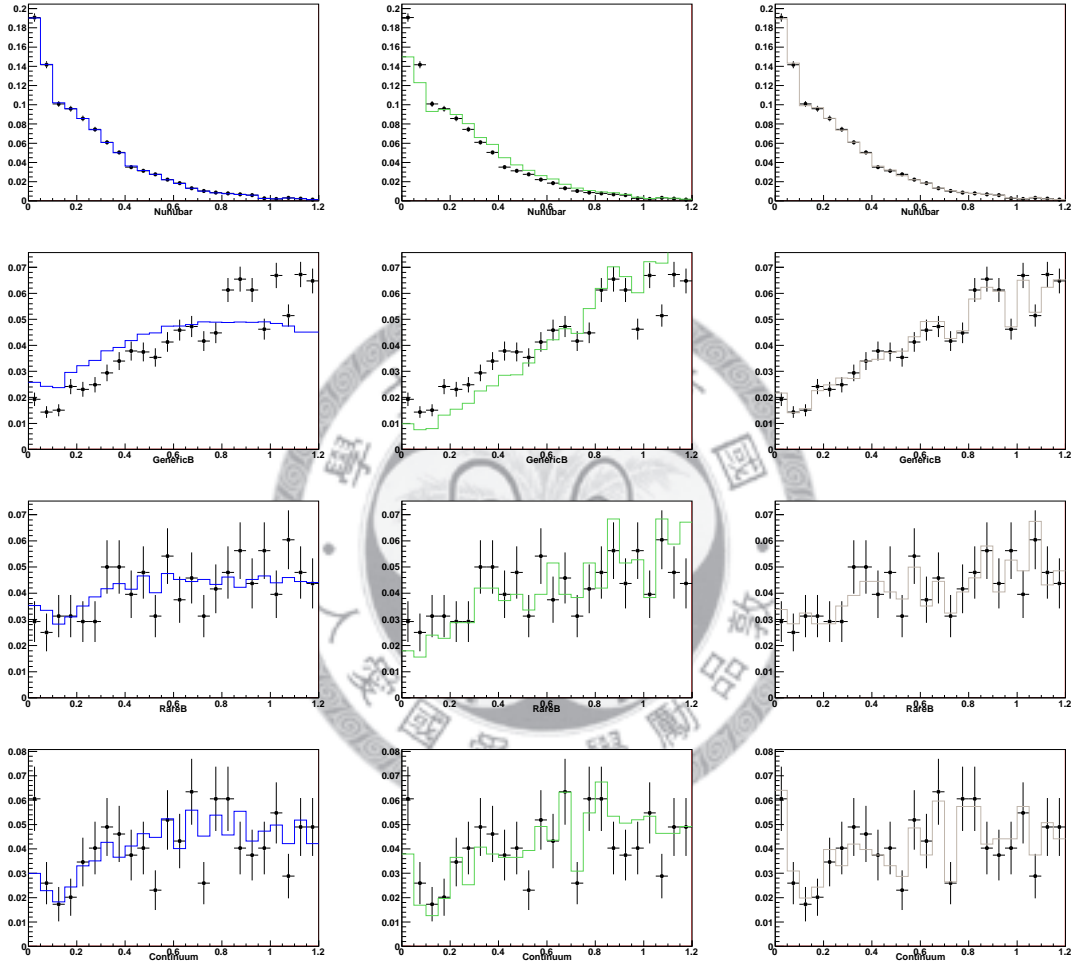
Figure 4.1: The comparison of PDF(point with error bar) and loose track veto(left)/loose π^0 veto(middle)/loose K_L veto(right) for E_{ECL} distribution. The E_{ECL} shapes for Non-B samples change a lot while loosening track and π^0 veto. The dramatic peak at zero becomes lower. From top to bottom, the order is signal, Generic$B$, Rare$B$, and Non-B samples.
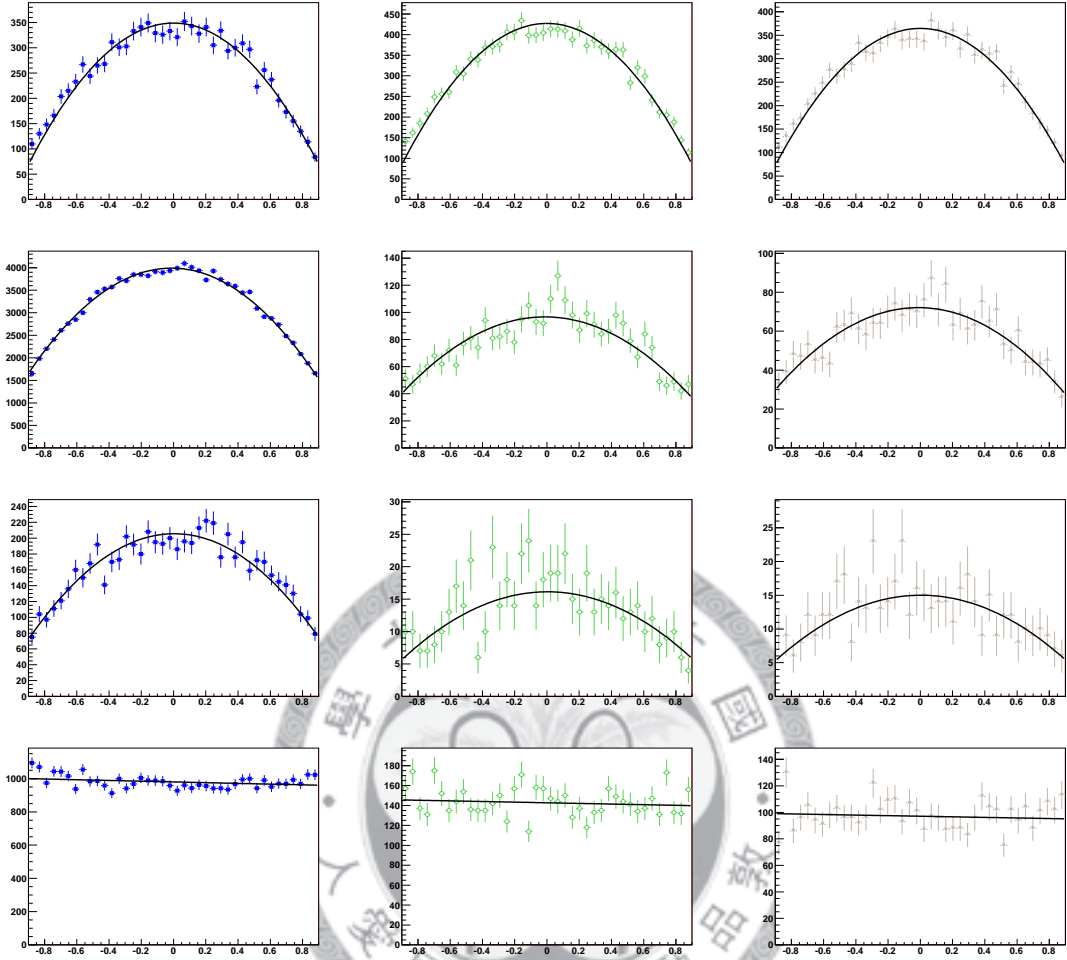
Figure 4.2: The comparison of PDF(solid line) and loose track veto(left/square with error bar)/loose π^0 veto(middle/circle with error bar)/loose K_L veto(right/square with error bar) for $\cos\theta_B$ distribution. From top to bottom, the order is signal, Generic$B$, Rare$B$ and Non-B samples.
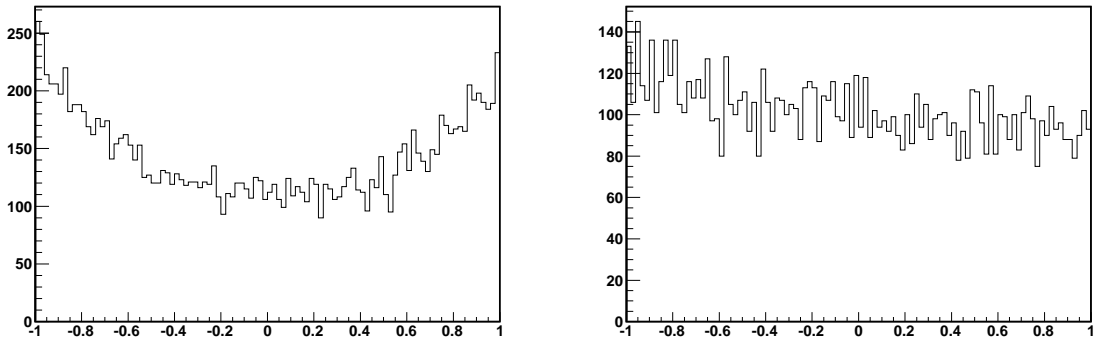
Figure 4.3: The distribution of $\cos\theta_B$ for continuum and Generic$B$ MC in $5.2 < M_{\rm bc} < 5.25$ region.
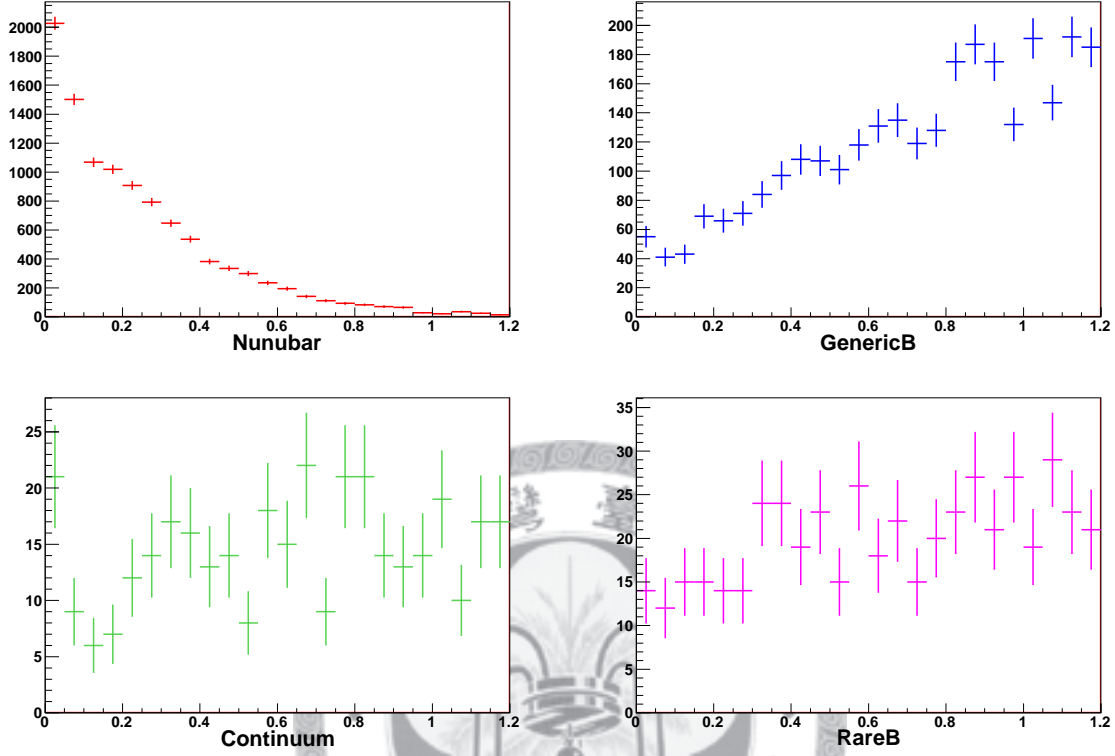
Figure 4.4: The E_{ECL} PDFs for signal, GenericB($b \to c$), Non-B(from off-resonance data) and RareB($b \to nonc$) samples.

Table 4.2: The PDF for E_{ECL} and $\cos \theta_B$.

	PDF	Function	Source
Signal	E_{ECL}	Discrete Histogram	MC
	$\cos \theta_B$	2nd Legendre P.	
Generic B	E_{ECL}	Discrete Histogram	MC
	$\cos \theta_B$	2nd Legendre P.	
Rare B	E_{ECL}	Discrete Histogram	MC
	$\cos \theta_B$	2nd Legendre P.	
Non-B	E_{ECL}	Discrete Histogram	Off-resonance Data
	$\cos \theta_B$	1st Legendre P.	MC
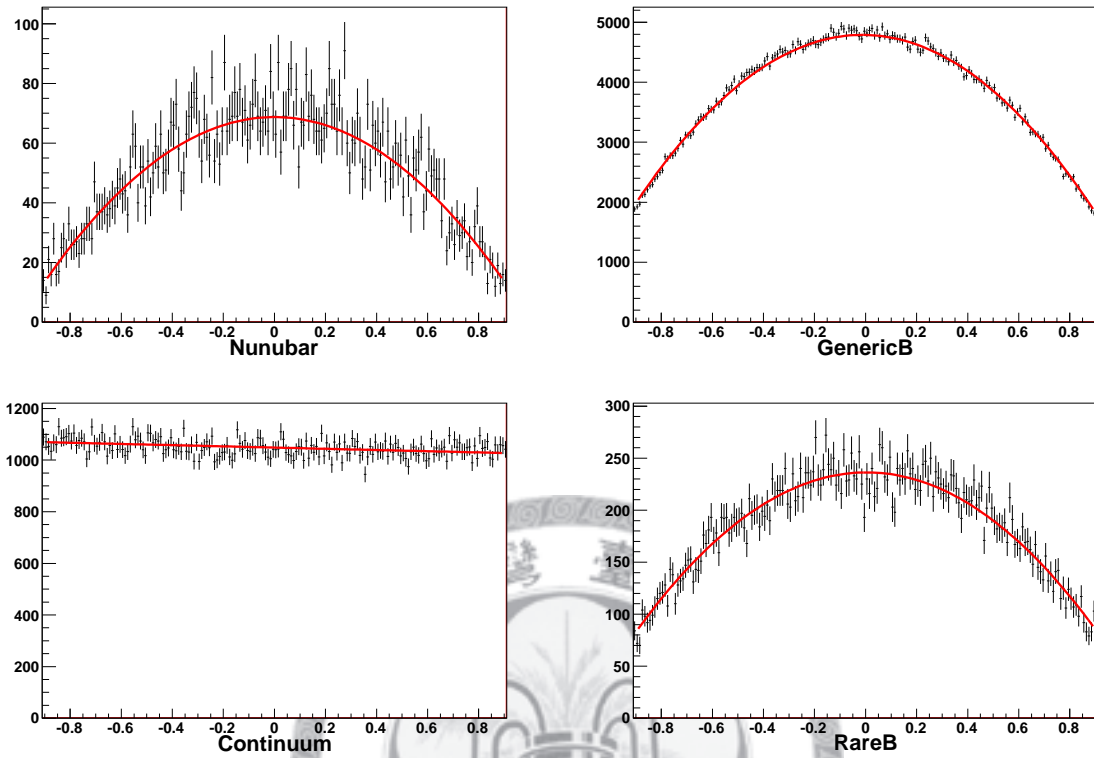
Figure 4.5: The $\cos\theta_B$ PDFs for signal, GenericB($b \to c$), Non-B and RareB($b \to nonc$) samples(from left to right, top to bottom). The red lines indicate the function for model PDF modelling.
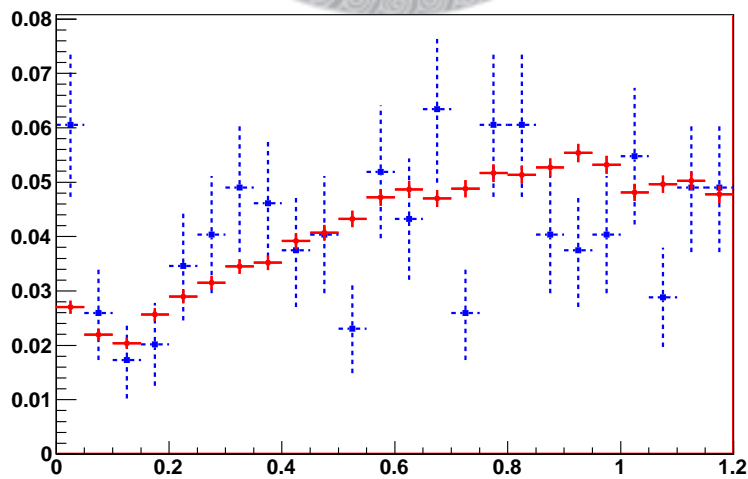
Figure 4.6: The overlap of E_{ECL} distribution in off-resonance data and continuum MC. The solid line indicates continuum MC, and the dash line indicates off-resonance data.

$\cos\theta_B$, e.g. $P(E_{ECL}, \cos\theta_B) = P(E_{ECL}) \times P(\cos\theta_B)$.
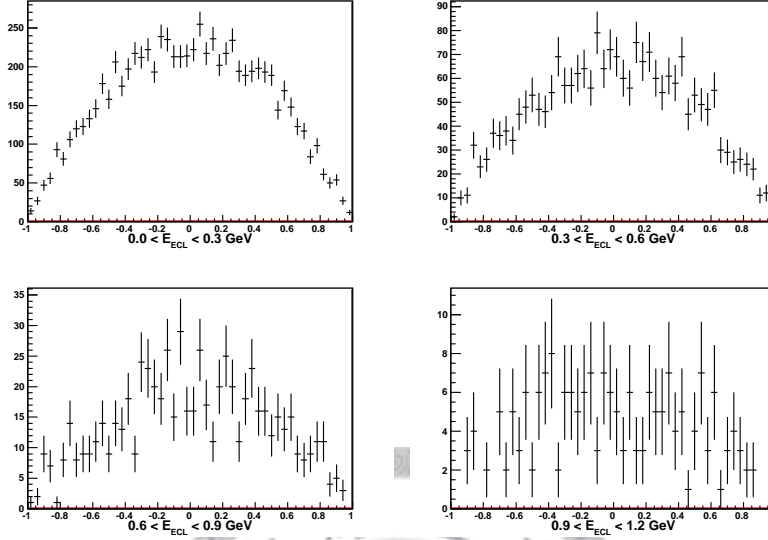
Figure 4.7: The distributions of $\cos\theta_B$ for signal MC sample in different E_{ECL} regions.

4.1.2   Null Signal Test with toy MC

In order to verify the validity of the fitter, we apply an ensemble test. We plot the distribution of yield, error, and fitting bias defined as

$$\text{Pull} = \frac{\text{Fit Number} - \text{Input Number}}{\text{Fit Error}}. \tag{4.2}$$

The mean value of pull distribution should be close to 0, and the sigma should be less than 1. For the distributions of yield and fitting error, the mean value of yield must be near the input number, and the sigma of yield is close to the mean of fitting error.

We generate 3000 sets of data via toy MC, and the number of events in each set base on the expected events shown in Table 3.3. The number of Rare B events is fixed in fit. The Fig 4.11 shows the fit result to the null signal sample. The result of ensemble test in yield/error/pull are $0.1229 \pm 0.1366/7.120 \pm 0.01/0.004 \pm 0.019$. Table 4.3 shows the result of yield in signal and background samples.
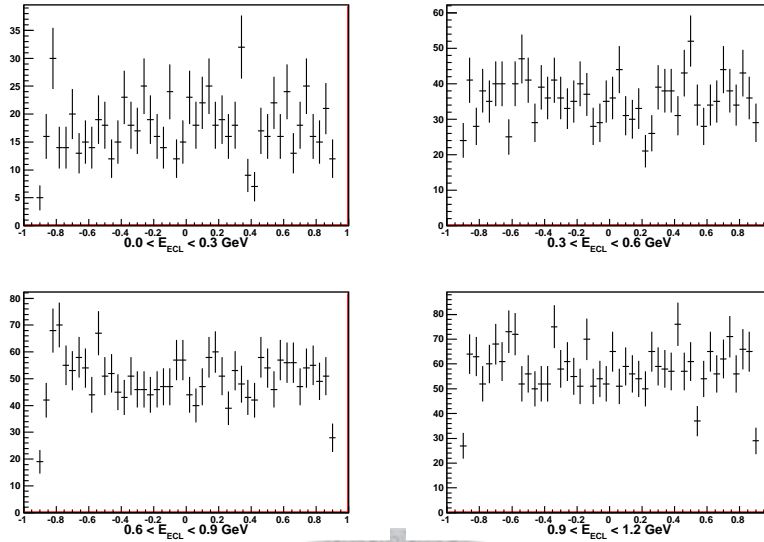
Figure 4.8: The distributions of $\cos\theta_B$ for continuum MC sample in different E_{ECL} regions.

Table 4.3: The yield of signal and background in toy MC test. There are five sources of backgrounds, but we fix the number of Rare B events in fit. There is no bias in both signal and background in fit.

	The Poisson distribution mean of events in sample	Fitting yield	Error
Signal	0	0.004	0.019
Generic B	67	66.33	0.53
Continuum	64	63.34	0.63

4.1.3 Toy MC test with the distribution of events in signal box

Since the PDFs is not constructed with the events in the signal box, we do a test using the events from toy MC generation based on the distributions of Generic$B$ MC with the signal box selection instead of original Generic$B$ PDFs. Note that we still use the same PDFs to fit. The result of yield/error/pull distribution are shown in Fig. 4.12, and the yields of signal, continuum, and Generic MC are shown in Fig. 4.13. We found a 4 events offset for signal yield in $N_{\text{signal}} = 0$ case (with expected statistic error 7.12). However, since the uncertainty of the 4 events offset could not be determined from toyMC and the expect statistic error is large, the bias would not be considered in the final result.
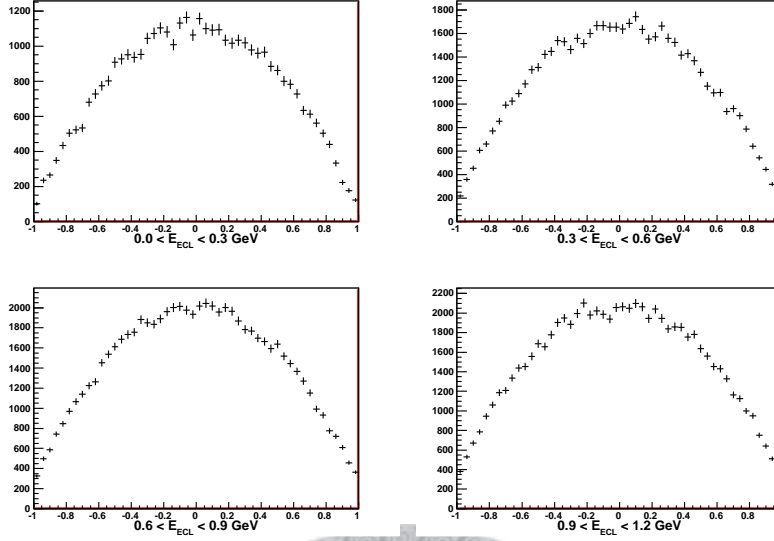
Figure 4.9: The distributions of $\cos\theta_B$ for Generic $B\overline{B}$ MC sample in different E_{ECL} regions.

4.2   Systematic uncertainties of Signal Yield

The source of systematic uncertainties in this analysis are listed below.

- **Uncertainty of the number of $B\overline{B}$ pairs**

  The number of $B\overline{B}$ pairs used in this analysis is $(656.725 \pm 8.940) \times 10^6$, thus an error of 1.4% is included.

- **Uncertainty of the tagging efficiency**

  The systematic error associated with the full-reconstruction tags are checked by B_{tag} candidates. The number of B yields are extracted by fits to the B_{tag} $M_{\rm bc}$ distributions, and the difference between data and the corresponding MC (a proper mixture of Generic $B\overline{B}$ and continuum events) is considered as a source of systematic uncertainty. Figure 4.15 shows the fits to neutral B samples, and the ratio between MC and data are given by

$$\frac{N_{MC}}{N_{data}} = 0.921 \pm 0.003. \tag{4.3}$$
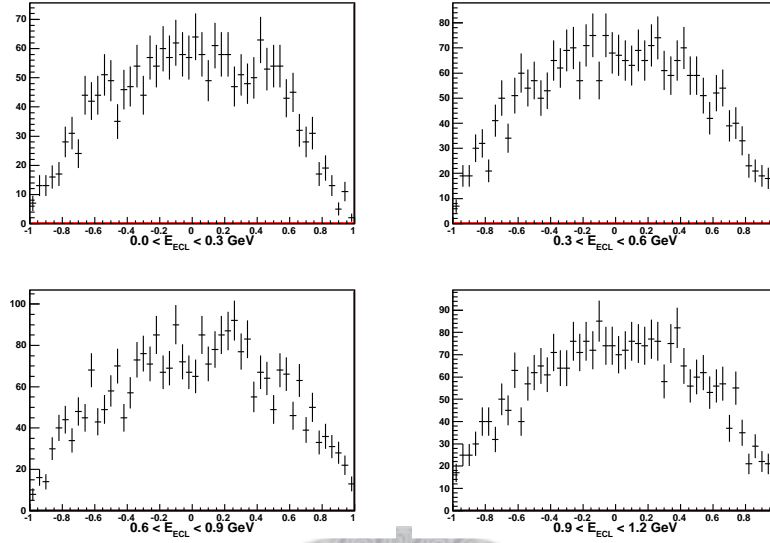
Figure 4.10: The distributions of $\cos\theta_B$ for Rare$B$ MC sample in different E_{ECL} regions.
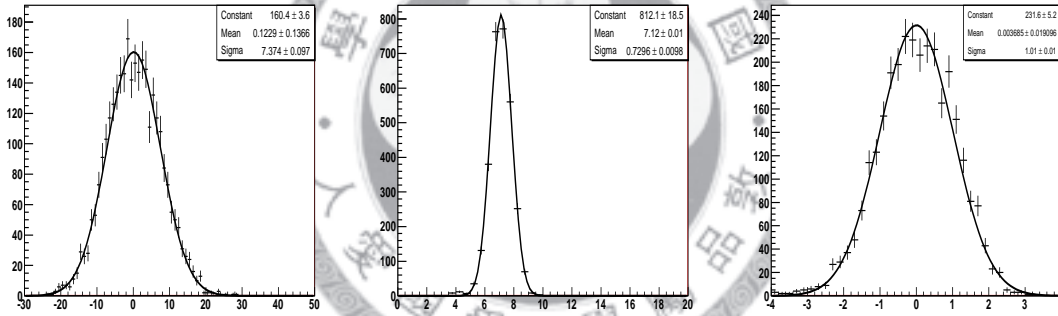
Figure 4.11: The mean, fitting error and pull distribution (from left to right) of the fitter in toy MC test.

The central shift plus 1σ statistic error is quoted as the systematic error for the tagging efficiency.

- **Uncertainty of the veto efficiency**

  The veto efficiency(track, π^0 and K_L vetoes) is checked by the control samples. The study of veto efficiencies is already described in Chap. 3.7. As we mentioned in chap 3.7, the averaged statistic error will be quoted as the systematic uncertainty. The track/π^0/K_L vetoes give the systematic uncertainty of 1.6%/2.0%/2.0%(Table 3.7). Te total error of veto efficiency is obtained by quadratically summing the error of
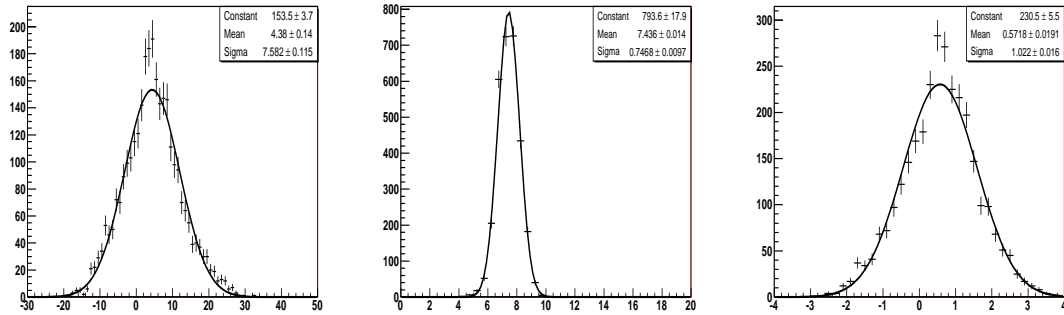
Figure 4.12: The mean, fitting error and pull distribution (from left to right) in the toyMC test.
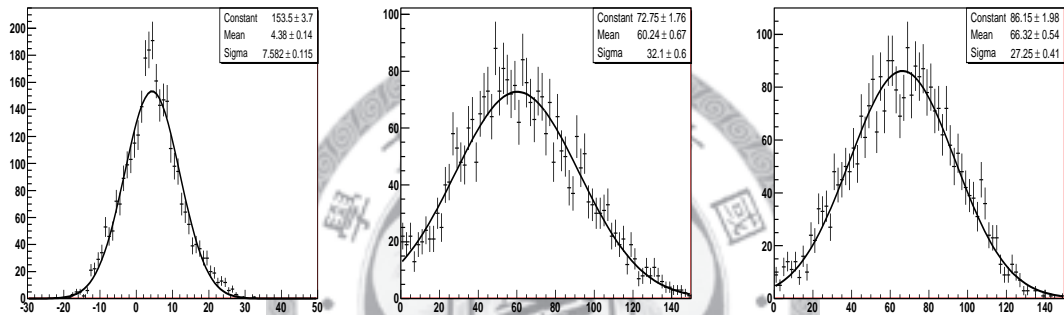
Figure 4.13: The yield of signal, continuum and GenericB components in the toy MC test with tighter selection PDFs. We a 4 events offset which might be due to the discrepancy between PDFs and the shape of events in signal box.

each terms, thus there is a systematic uncertainty of 3.2% from veto efficiency.

- **Uncertainty of the PDF modelling**

  The systematic uncertainty due to statistic error of the PDF modelling is estimated by changing each bin contents of the histogram by $\pm 1\sigma$ and repeating the fit. There are 24 bins, so we fit 24×2 times and add all the deviations in quadrature. For the non-B PDF, the binning effect is also considered. The systematic uncertainty from PDF modelling are listed in Table 4.4.

A summary of the systematic uncertainties is given by the Table 4.5.

Table 4.4: Summary of uncertainty from PDF modelling. Note that the PDF modelling uncertainty is in the unit of event numbers.

Sources	Syst. uncertainty(Events)
Signal	negligible
Generic$B$ BG	$^{+1.6}_{-1.4}$
Rare$B$ BG	± 0.1
Non-B BG	$^{+1.9}_{-1.3}$
Non-B BG(binning effect)	$^{+0.0}_{-1.8}$
Sum	$^{+2.5}_{-2.6}$
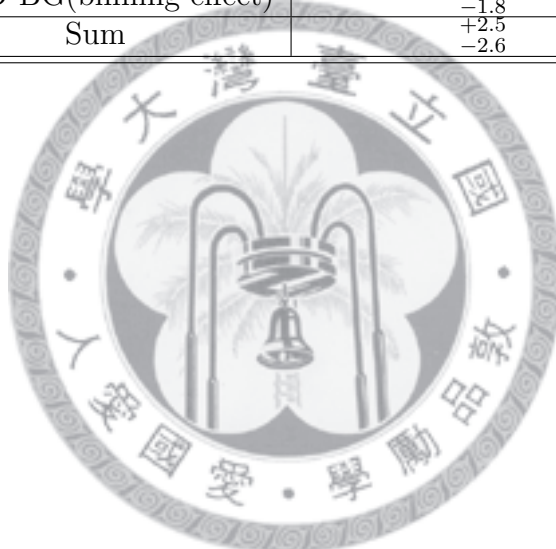
Table 4.5: Summary of systematic uncertainties(%). Note that the PDF modelling uncertainty is in the unit of event numbers.

Sources	Syst. uncertainty
$N(B\overline{B})$	1.4%
Tagging eff.	8.3%
Track veto eff.	1.6%
π^0 veto eff.	2.0%
K_L veto eff.	2.0%
Sum	9.0%
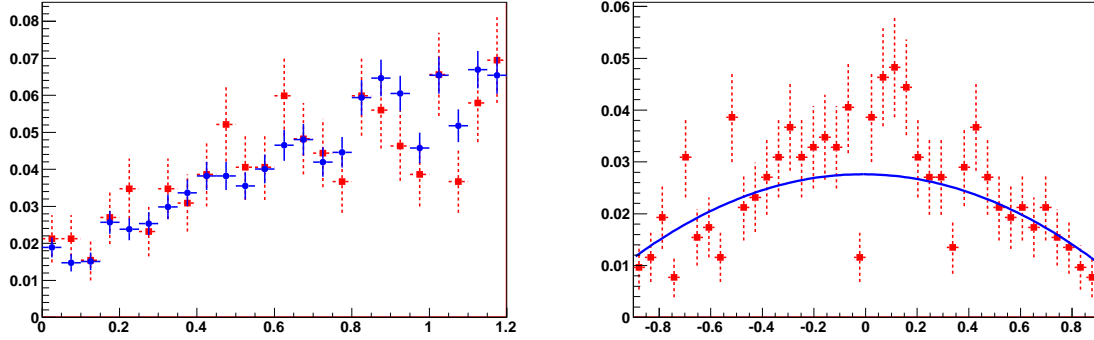
Figure 4.14: The comparison of E_{ECL}(left) and $\cos\theta_B$(right) distribution in PDF selection and signal box on Generic$B$ MC. The red point denotes the signal box events, and the blue one indicates PDF.

4.3   Upper Limit Estimation

The expected upper limit can be estimated by the fitting error obtained from pull test. Considering the statistic error is 7 ,$N_{\text{signal}} = 0$ with systematic error(9.0% and 4 events bias), calibration factor(-5.4% for π^0 veto and 9.6% for K_L veto) and signal efficiency(2.2×10^{-4}). The estimation of upper limit is 1.0×10^{-4}.

4.4   Fit Result

After finalizing the signal selection criteria, we examine the signal yield. Figure 4.16 show the E_{ECL} and $\cos\theta_B$ distributions with the fit result, and Table 4.6 shows the yields in data. We found no significant excess. The obtained signal yield is

$$N_{sig} = 8.9^{+6.3}_{-5.5}(stat)^{+2.6}_{-2.7}(syst). \tag{4.4}$$

The first and second error are the statistic and the systematic uncertainties, respectively.

MINUIT Likelihood Fit to Plot 21&0

mc
File: final.hbk   13-JUN-2011 23:33
Plot Area Total/Fit   3.14823E+06 / 3.14823E+06   Fit Status 3
Func Area Total/Fit   3.14831E+06 / 3.14831E+06   E.D.M. 5.171E-08
Likelihood = 1078.7
χ^2 = 947.0 for 400 - 9 d.o.f.,   C.L.= 0.00 %

Errors		Parabolic		Minos
Function 1: Gaussian (sigma)				
AREA	4.06210E+05	± 1750.	- 1747.	+ 1752.
MEAN	5.2805	± 8.1593E-06	- 8.1546E-06	+ 8.1459E-06
SIGMA	2.79201E-03	± 9.1272E-06	- 9.1198E-06	+ 9.1281E-06
Function 2: ARGUS Background				
NORM	6.95047E+07	± 1.5686E+06	- 1.5706E+06	+ 1.5525E+06
OFFSET	-1.00136E-04	± 5.4121E-10	- 1.9353E-10	+ 0.000
*EBEAM	5.2900	± 0.000	- 0.000	+ 0.000
EFACT	-16.116	± 0.7331	- 0.7220	+ 0.7389
Function 3: ARGUS Background				
NORM	7.87028E+07	± 1.6511E+06	- 1.6487E+06	+ 1.6465E+06
OFFSET	2.42917E-04	± 9.5626E-06	- 9.9484E-06	+ 0.000
*EBEAM	5.2900	± 0.000	- 0.000	+ 0.000
EFACT	-134.52	± 2.992	- 3.013	+ 2.942

$N_{MC} = 406150 \pm 1750$
B^0 tagged MC

MINUIT Likelihood Fit to Plot 20&0

data
File: final.hbk   13-JUN-2011 23:30
Plot Area Total/Fit   3.25146E+06 / 3.25146E+06   Fit Status 3
Func Area Total/Fit   3.25152E+06 / 3.25152E+06   E.D.M. 5.797E-10
Likelihood = 941.6
χ^2 = 809.5 for 400 - 9 d.o.f.,   C.L.= 0.00 %

Errors		Parabolic		Minos
Function 1: Gaussian (sigma)				
AREA	4.40873E+05	± 1777.	- 1774.	+ 1779.
MEAN	5.2807	± 7.9483E-06	- 7.4757E-06	+ 7.4680E-06
SIGMA	2.70331E-03	± 8.4021E-06	- 8.3954E-06	+ 8.4047E-06
Function 2: ARGUS Background				
NORM	6.80409E+07	± 1.4552E+06	- 1.4724E+06	+ 1.4523E+06
OFFSET	-1.00135E-04	± 5.5611E-14	- 0.000	+ 0.000
*EBEAM	5.2900	± 0.000	- 0.000	+ 0.000
EFACT	-13.518	± 0.7168	- 0.7120	+ 0.7299
Function 3: ARGUS Background				
NORM	8.90936E+07	± 1.4830E+06	- 1.4990E+06	+ 1.4959E+06
OFFSET	2.45461E-04	± 8.8354E-06	- 8.6298E-06	+ 7.9733E-06
*EBEAM	5.2900	± 0.000	- 0.000	+ 0.000
EFACT	-142.58	± 2.983	- 3.010	+ 2.958

$N_{data} = 440802 \pm 1777$
B^0 tagged data

Figure 4.15: Systematic studies for the full-reconstruction tags. Fits to the B_{tag} M_{bc} distributions are performed for MC and data.

Table 4.6: Fit results of yields in data. Note that the Rare$B$ BG is fixed in fit.

Sources	Yield
Signal	$8.9^{+6.3}_{-5.5}$
Generic$B$ BG	$131.6^{+21.9}_{-22.8}$
Non-B BG	$-23.2^{+21.6}_{-17.0}$
Rare$B$ BG	3.7
Total	121
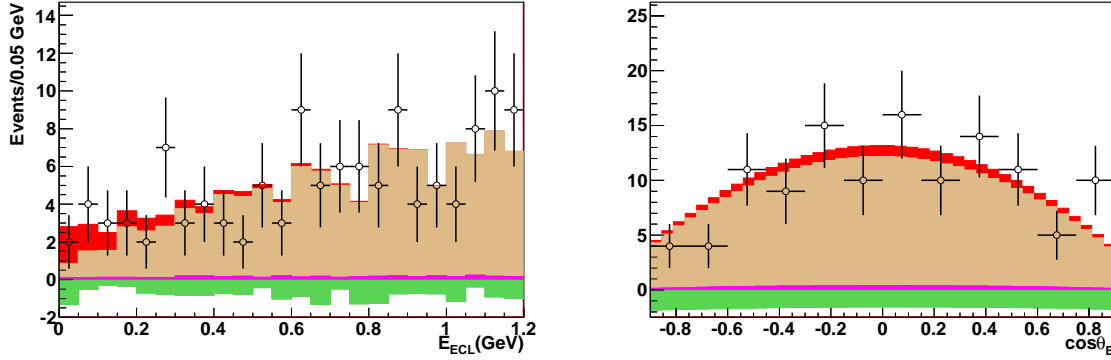
Figure 4.16: The E_{ECL}(left) and $\cos\theta_B$(right) distributions with fit results. The points with error bar are data. The red region is signal PDF, brown is Generic$B$, green for non$B$ and pink for Rare$B$. From the fit result, we don't find any entry for non-B event.

4.5 Branching fraction upper limit estimation

Because the $B \to invisible$ decay is not significant, we evaluate the upper limit at 90% confidence level. The upper limit on the B yield, N, is obtained by integrating the likelihood function $\mathcal{L}(n)$:

$$\int_0^N \mathcal{L}(n)dn = 0.9 \int_0^\infty \mathcal{L}(n)dn,$$ (4.5)

where n denotes to the signal yield.

The systematic error are taken into account by smearing the likelihood function with a gaussian which width is the systematic uncertainty,

$$\mathcal{L}_{smear}(N_{sig}) = \int \mathcal{L}(N'_{sig}) \frac{e^{-\frac{(N_{sig} - N'_{sig})^2}{2\Delta N_{sig}^2}}}{\sqrt{2\pi\Delta N_{sig}}} dN'_{sig}.$$ (4.6)

Figure 4.17 shows the likelihood distributions before and after smearing.

Finally, we determine the branching fraction $\mathcal{B}(B \to invisible) < 1.3 \times 10^{-4}$ at the 90% C.L.
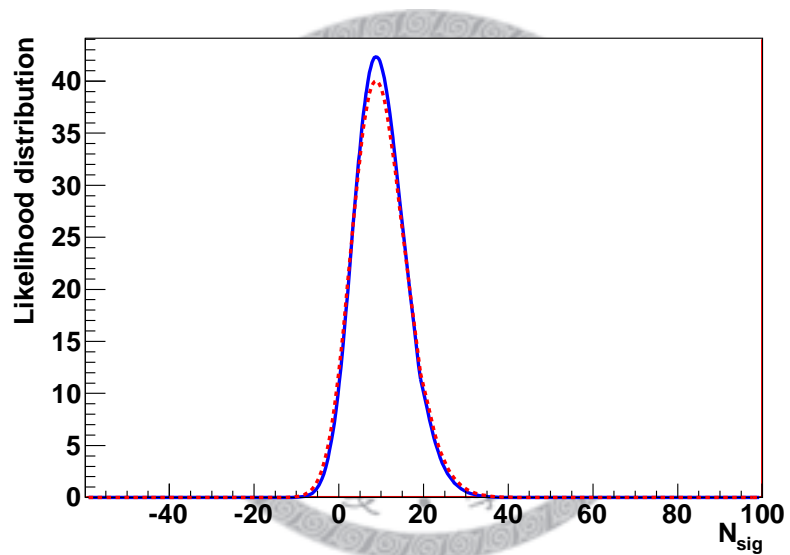
Figure 4.17: The likelihood function for $B \to invisible$ decay. The red dash line and blue solid line are likelihood distribution after and before smeared, respectively.

Appendix A

Optimazation of E_{ECL} threshold

Since the E_{ECL} variable is the most powerful one to distinguish signal and background events, finding the best threshold for ECL clusters can avoid the fake signal which was caused by the electronic or the beam background.

In the previous similar analysises at Belle, the default value of ECL threshold as the following.

- $E_{ECL} > 0.05$ GeV (barrel)

- $E_{ECL} > 0.10$ GeV (forward end-cap)

- $E_{ECL} > 0.15$ GeV (backward end-cap)

However, the backward threshold is greater than the forward one. In this section, we tried to find the reason for the higher threshold on backward part, and optimize the energy on ECL cluster with different threshold sets.

A indirect evidence is the DQM plot of ECL information. From the DQM plot, Fig A.1, the backward crystals are suffered more radiations from the beam background than the forward part. Hence, it is necessary to put a higher threshold on the backward end-cap.
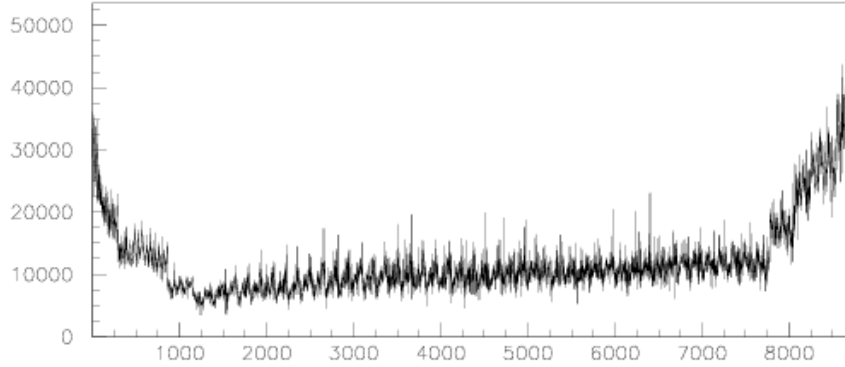
ECL plot 3: hit map, TDC low, for energy $> 2\,\mathrm{MeV}$ (raw)

Figure A.1: DQM plots. The backward end-cap is suffered more radiations than the forward.

Then we optimized the threshold requirement by using the background PDF(Generic MC, continuum MC, and tau-pair MC) of the main analysis in the B_{tag} M_{bc} sideband region and the signal PDF from $B \to D^* \mu \nu$ study in the B_{tag} signal region. The B_{tag} M_{bc} sideband region is defined as $5.2 < M_{\mathrm{bc}} < 5.25 (\mathrm{GeV}/c^2)$, and the B_{tag} signal region is $5.27 < M_{\mathrm{bc}} < 5.29 (\mathrm{GeV}/c^2)$ with $-0.08 < \Delta E < 0.06 (\mathrm{GeV})$

To optimize the threshold energy, we divide both end-cap regions into five bins equally by the θ angle of the ECL cluster, and assume the threshold energy is linear dependent with the θ angle. The six trial threshold energy sets are listed in Table A.1

For the purpose of measuring the separateness of signal and background events, the χ^2 variable is introduced. The definition of χ^2 is

$$\chi^2 = \sum_{i=1}^{r} \frac{(N \cdot m_i - M \cdot n_i)^2}{M^2 \cdot n_i + N^2 \cdot m_i}, [25] \tag{A.1}$$

where m_i, n_i mean the content of ith bin, and M, N present the summation of m_i, n_i. In this study, n_i is for signal PDF and m_i is for background PDF. But the result is the same even we exchange the definition of n_i and m_i. We choose threshold cuts with the largest χ^2 so that the signal and background could be separated best. The result shows in Table A.3.

According to this result, the default ECL energy threshold which gives best separating power is applied. Energy thresholds of 50/100/150 MeV are required for photons in the barrel/forward end-cap/backward end-cap respectly.

Table A.1: Six trial threshold energy sets with corresponding θ region in forward end-cap

Trial Sets	Threshold energy on Forward end-cap(MeV)				
	12.4°∼ 16.2°	16.2°∼ 19.9°	19.9°∼ 23.7°	23.7°∼ 27.5°	27.5°∼ 31.4°
A	200	162.5	125	87.5	50
B	250	200	150	100	50
C	300	237.5	175	112.5	50
D	250	212.5	175	137.5	100
E	350	275	200	125	50
F	150	125	100	75	50

Table A.2: Six trial threshold energy sets with corresponding θ region in backward end-cap

Trial Sets	Threshold energy on Backward end-cap (MeV)				
	130.7°∼ 135.6°	135.6°∼ 140.4°	140.4°∼ 145.3°	145.3°∼ 150.2°	150.2°∼ 155.1°
A	50	100	150	200	250
B	50	112.5	175	237.5	300
C	50	125	200	275	350
D	100	150	200	250	300
E	50	137.5	225	312.5	400
F	50	87.5	125	162.5	200

Table A.3: Trial set and its χ^2/degree of freedom, here the degree of freedom is 23(there are 24 bins in each plots)

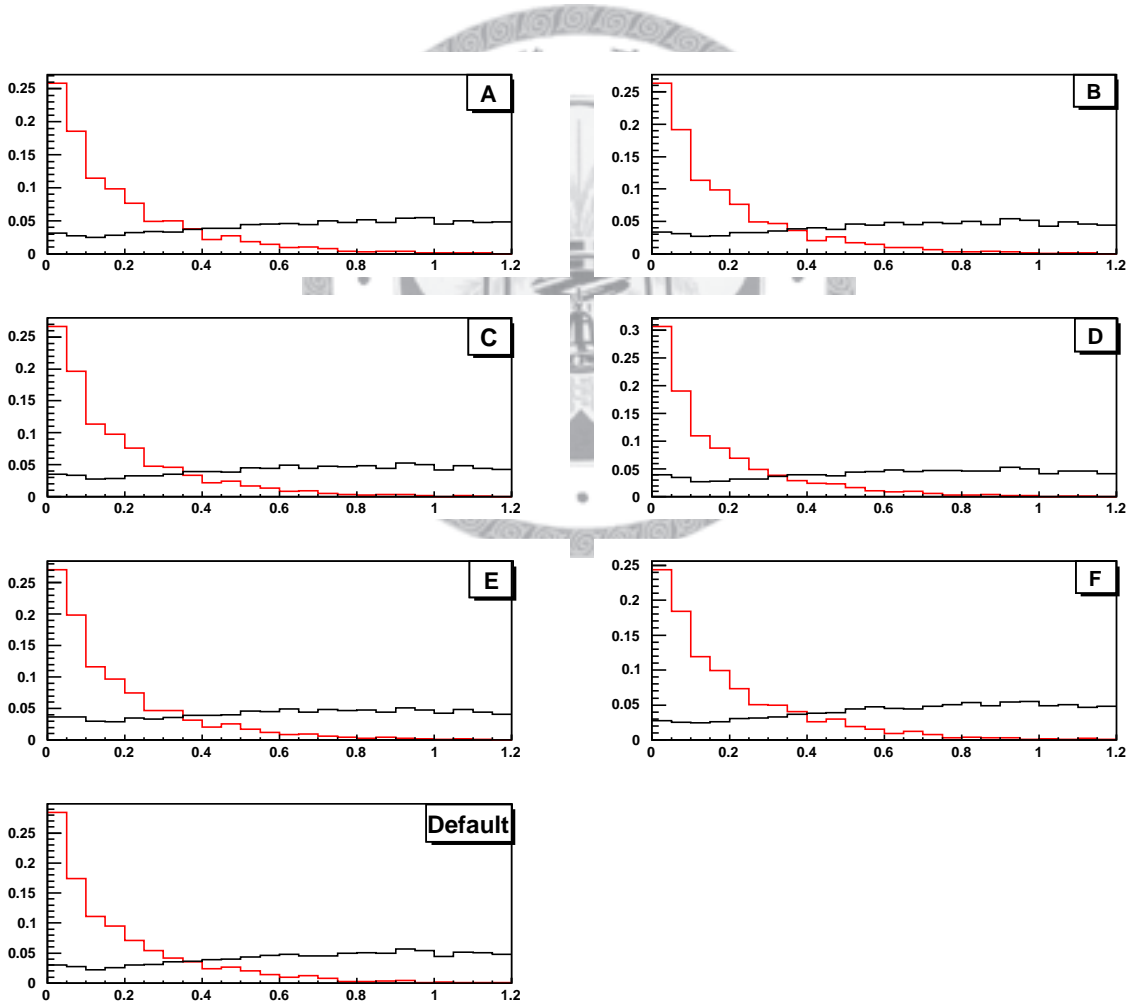|	χ^2/degree of freedom
A	0.0405
B	0.0399
C	0.0392
D	0.0401
E	0.0390
F	0.0408
Default	0.0414

Figure A.2: The normalized histogram for ECL threshold study, red curves mean signal MC of $B^0 \rightarrow D^*\mu\nu$, black lines indicate the combination of GenericB, continuum and tau-pair background PDFs for the main analysis.

Bibliography

[1] Nakamura, K. et al. *J. Phys.* **G37**, 075021 (2010).

[2] Sakharov, A. D. *Pisma Zh. Eksp. Teor. Fiz.* **5**, 32–35 (1967).

[3] Lee, T. D. and Yang, C. N. *Phys. Rev.* **104**(1), 254–258 Oct (1956).

[4] Wu, C. S., Ambler, E., Hayward, R. W., Hoppes, D. D., and Hudson, R. P. *Phys. Rev.* **105**(4), 1413–1415 Feb (1957).

[5] Christenson, J. H., Cronin, J. W., Fitch, V. L., and Turlay, R. *Phys. Rev. Lett.* **13**(4), 138–140 Jul (1964).

[6] Cabibbo, N. *Phys. Rev. Lett.* **10**(12), 531–533 Jun (1963).

[7] Kobayashi, M. and Maskawa, T. *Progress of Theoretical Physics* **49**(2), 652–657 (1973).

[8] Herb, S. W. et al. *Physical Review Letters* **39**, 252–255 August (1977).

[9] Bienlein, J. K. et al. *Physics Letters B* **78**(2-3), 360 – 363 (1978).

[10] Andrews, D. et al. *Phys. Rev. Lett.* **45**(4), 219–221 Jul (1980).

[11] Agashe, K., Deshpande, N. G., and Wu, G. H. *Physics Letters B* **489**(3-4), 367 – 376 (2000).

[12] Agashe, K. and Wu, G.-H. *Physics Letters B* **498**(3-4), 230 – 236 (2001).

[13] Davoudiasl, H., Langacker, P., and Perelstein, M. *Phys. Rev. D* **65**(10), 105015 May (2002).

[14] Buchalla, G. and Buras, A. J. *Nuclear Physics B* **400**(1-3), 225 – 239 (1993).

[15] Dedes, A., Dreiner, H., and Richardson, P. *Phys. Rev. D* **65**(1), 015001 Nov (2001).

[16] Adams, T. et al. *Phys. Rev. Lett.* **87**(4), 041801 Jul (2001).

[17] Aubert, B. et al. *Phys.Rev.Lett.* **93**, 091802 (2004).

[18] Abashian, A. et al. *Nuclear Instruments and Methods in Physics Research Section A: Accelerators, Spectrometers, Detectors and Associated Equipment* **479**(1), 117 – 232 (2002).

[19] Kawasaki, T. *Nuclear Instruments and Methods in Physics Research Section A: Accelerators, Spectrometers, Detectors and Associated Equipment* **494**(1-3), 94 – 101 (2002).

[20] Lange, D. J. *Nucl. Instrum. Meth.* **A462**, 152–155 (2001).

[21] Brun, R. and et.al. *CERN Report* **DD/EE//84-1** (1986).

[22] Hanagaki, K. et al. *BELLE Note 312* (2000).

[23] Piilonen, L. et al. *BELLE Note 338* (2000).

[24] Kumar, S. *BELLE Note 351* (2000).

[25] Gagunashvili, N. D. *ArXiv Physics e-prints* May (2006).